

The calm before the (next) storm: no third outburst in 2019–2020, and ongoing monitoring of the transient AGN IC 3599

DIRK GRUPE,¹ S. KOMOSSA,² AND SALEM WOLSING¹

¹*Northern Kentucky University, Department of Physics, Geology, and Engineering Technology, Nunn Drive, Highland Heights, KY 41099, USA*

²*Max-Planck-Institut für Radioastronomie, Auf dem Hügel 69, 53121 Bonn, Germany*

(Received 2024 February 29; Accepted 2024 April 18)

ABSTRACT

We report on follow-up observations of the Seyfert 1.9 galaxy IC 3599 with the NASA Neil Gehrels *Swift* mission. The detection of a second X-ray outburst in 2010 by *Swift* after the first discovery of a bright X-ray outburst in 1990 by ROSAT led to the suggestion of two very different explanations: The first one assumed that IC 3599 exhibits outbursts due to repeated partial tidal stripping of a star, predicting another outburst of IC 3599 in 2019/2020. The second, alternative scenario assumed that the event observed in X-rays is due to an accretion disk instability which would suggest a much longer period between the large outbursts. Our continued monitoring campaign by *Swift* allowed us to test the first scenario which predicted a repetition of high amplitude flaring activity in 2019/2020. We do not find any evidence of dramatic flaring activity with factors of 100 since the last X-ray outburst seen in 2010. These observations support the accretion disk scenario. Further, while IC 3599 remains in low emission states, the long-term X-ray light curve of IC 3599 reveals ongoing strong variability of a factor of a few. The most remarkable event is a mini flare of a factor of 10 in X-rays in December 2022. After that flare, the otherwise supersoft X-ray spectrum shows an exceptional hardening, reminiscent of a temporary corona formation.

Keywords: active galactic nuclei – supermassive black holes – X-rays: galaxies – ultraviolet: galaxies – quasars: individual (IC 3599)

1. INTRODUCTION

Since the proposed scenario of the tidal disruption of a stars by a supermassive black holes (e.g., Rees 1988), there have been many observations confirming this scenario. In the 1990s the X-ray mission ROSAT (Truemper 1982) had been instrumental for the discovery of the first stellar tidal disruption events (TDEs), in the form of giant-amplitude X-ray outbursts from quiescent host galaxies (e.g., NGC 5905 (Bade et al. 1996; Komossa & Bade 1999), RX J624.9+7554 (Grupe et al. 1999), and RX J1242.6–1119 (Komossa & Greiner 1999)). More recently, TDEs have been detected by all major X-ray observatories, including the discovery of jetted events with the Neil Gehrels Swift observatory, first in Swift J164449.3+573451 (e.g., Burrows et al. 2011; Bloom et al. 2011; Zauderer et al. 2011). The discovery of TDEs from quiescent galaxies, however, is not limited to the X-ray sky. GALEX led to the first detection of events in the UV-optical band (Gezari et al.

2006), and SDSS enabled the first identification of events with transient optical emission lines such as HeII, broad Balmer lines, and coronal lines (Komossa et al. 2008). TDE candidates continue to be identified at all wavebands (see Komossa 2015; van Velzen et al. 2021; Webb et al. 2023; Komossa & Grupe 2023, for recent reviews).

Although the TDE model is required to explain sudden, luminous X-ray outbursts in *non-active* galaxies, this picture is far from being clear in AGN. In the case of an AGN, the power is coming from a long-lived accretion disk surrounding the central supermassive black hole. This power is not constant and varies, and in extreme cases a significant change in the disk properties can cause a dramatic increase in the AGN luminosity. An increasing number of optical changing-look AGN which do change their luminosity output along with their optical broad emission lines, have been identified in recent years (see Komossa & Grupe 2023, for a review) even though the first cases were known already

in the 1970s–80s (e.g., Penston & Perez 1984; Alloin et al. 1985). Different theoretical scenarios related to accretion disk instabilities or other disk processes have been explored in recent years (e.g., Nicastro 2000; Grupe et al. 2015; Ross et al. 2018; Noda & Done 2018; Dexter & Begelman 2019; Sniegowska et al. 2020; Pan et al. 2021; Kaaz et al. 2023; Cao et al. 2023). There will be a major discovery space for both, TDEs and changing-look AGN once the Vera Rubin Telescope will go online¹.

One of the earliest examples of an AGN that might have exhibited either a TDE or an accretion disk instability was the Seyfert 1.9 galaxy IC 3599 (Zw 159.034; 1RXS J123741.2+264227; $\alpha_{2000} = 12^{\text{h}}37^{\text{m}}41.^{\text{s}}2$, $\delta_{2000} = +26^{\circ}42'27''$, $z=0.0215$). IC 3599 was discovered as a very X-ray bright AGN during the ROSAT All-Sky Survey (RASS, Voges et al. 1999) in 1990. Subsequent pointed ROSAT observations during the following years revealed that it had faded by a factor of initially 60 and even more than 100 in later observations. Both, Brandt et al. (1995) and Grupe et al. (1995) speculated at the time that this was caused by either a TDE or high-amplitude AGN variability.

What made both scenarios plausible was the discovery of a strong evolution in the optical emission line spectrum. The spectrum taken about half a year after the RASS observation shown in Brandt et al. (1995) showed very strong permitted lines from Hydrogen and Helium along with transitions from other elements. These strong emission lines led Brandt et al. (1995) to classify IC 3599 as a Narrow-Line Seyfert 1 galaxy (NLS1), albeit without FeII emission. Grupe et al. (1995) showed spectra obtained years after the RASS which displayed the spectrum of a Seyfert 2 galaxy but with fading coronal iron lines. The fading coronal lines were confirmed by new optical spectroscopy of Komossa & Bade (1999) who still detected a broad component in $H\alpha$, making IC 3599 a Seyfert 1.9 galaxy. These authors re-emphasized that TDEs are best identified in quiescent host galaxies, because in AGN, accretion-disk-related activity is the most plausible explanation for variability Rees (see also 1990). Note, no FeII lines, the signature lines in Narrow Line Seyfert 1 galaxies, were present at any time in the optical data of IC 3599. Doubt remained given that this is an AGN, if a TDE really was an explanation of the X-ray outburst. Instead, the spectacular changes in its optical emission-line spectrum combined with the dramatic X-ray variability make IC 3599 one of the most extreme examples of a changing-look AGN (Komossa & Grupe 2023).

After ROSAT, IC 3599 was again observed in X-rays by Chandra in 2002 (Vaughan et al. 2004) and was still found in an X-ray low state. In two observations by the Neil Gehrels *Swift* mission (Gehrels et al. 2004, *Swift* hereafter) in 2010, it was seen again in an X-ray outburst state with its X-ray flux at a similar level as during the RASS (Grupe et al. 2015). Based on the RASS observation from 1991, the Chandra observation from 2002, and the *Swift* observation from 2010, Campana et al. (2015) speculated that the 2010 outburst was due to the tidal stripping of a star, repeating an initial 1991 tidal stripping event of a star orbiting the black hole, with a low black hole mass of $3 \times 10^5 M_{\odot}$ and a 9.5-year orbital period. This kind of repeated flaring has been suggested e.g. by Payne et al. (2021) to explain the quasi-periodic eruptions in ESO 253-G003/AT2014ko. Campana et al. (2015) predicted that another outburst in IC 3599 would be visible in 2019/2020. Although this is an intriguing model, Grupe et al. (2015) argued that the 1990 and the 2010 outbursts were due to accretion disk instabilities. Major arguments were the optical light curve from the Catalina observatory which showed a relatively gradual increase in the optical flux, as well as a low black hole mass not being supported by any observational parameter (instead, it was measured to be of the order of $2 - 20 \times 10^6 M_{\odot}$).

To test these different models, we continued to monitor IC 3599 with *Swift* typically once per month for a nine-month period each year. *Swift* is unable to observe IC 3599 for a three-month period between August and November due to the sun-constraint (a 45° sun avoidance angle). Here we report on the entire *Swift* monitoring campaign from 2010 to June 2023. During the entire monitoring period no further outbursts have been observed in IC 3599, supporting the accretion disk instability scenario suggested by Grupe et al. (2015). Over the last few years there has been, however, a general trend of IC 3599 slowly becoming brighter in X-rays, and it has recently been observed in an intermediate state.

This paper is organized as follows: in Section 2 we will describe the *Swift* observations, present the results in Section 3, and then discuss them in Section 4. Throughout the paper spectral indices are denoted as $F_{\nu} \propto \nu^{-\alpha}$. Luminosities are calculated assuming a Λ CDM cosmology with $\Omega_{\text{M}}=0.286$, $\Omega_{\Lambda}=0.714$ and a Hubble constant of $H_0=70 \text{ km s}^{-1} \text{ Mpc}^{-1}$, resulting in a luminosity distance of $D=91.4 \text{ Mpc}$ using the cosmology calculator by Wright (2006). All errors are 1σ unless stated otherwise.

¹ <https://rubinobservatory.org/>

Swift has observed IC 3599 since 2010. When it was discovered in 2013 that it had exhibited an X-ray outburst in 2010 (Grupe et al. 2015) we started observing it once a month. These observations were supported by another set of monthly observations (PI Campana) in 2019 which essentially made it a two-week cadence. All *Swift* observations are listed in Table 4. The full machine-readable table is available on Zenodo: [10.5281/zenodo.10899673](https://zenodo.org/record/10899673).

The *Swift* X-ray telescope (XRT; Burrows et al. 2005) was operating in photon counting mode (pc mode, Hill et al. 2005) and the data were reduced by the task *xrt-pipeline* which is part the HEASOFT package 6.30.1. Source counts were extracted in a circle with a radius of $47.1''$ (except the 2010 outburst observation for which we used $70.7''$). The background counts were extracted in a nearby circular region with a radius of $247.5''$. For all spectra we used the most recent response file *swxpc0to12s6_20130101v014.rmf*. The X-ray spectra were analyzed using *XSPEC* version 12.12.1 (Arnaud 1996). If a sufficient number of counts (>30) was available, we used W-statistics (Cash 1979) for single observations. Although often the number of counts was too low to allow for a spectral analysis, we still determined a hardness ratio, defined as $HR = \frac{\text{hard-soft}}{\text{hard+soft}}$ with the soft and hard bands in the 0.3-1.0 and 1.0-10 keV range, respectively by applying the program by Park et al. (2006). The count rates in the XRT were determined by using the *Swift* XRT product page at the *Swift* Data Center at the University of Leicester² (Evans et al. 2007), as well as the Living Swift XRT Point Source Catalogue³ (Evans et al. 2023).

To perform a spectral analysis of different X-ray flux states, we merged the data of various time period into single data sets within XSELECT. These periods and spectral analysis results are listed in the appendix in Table 2. We then constructed the auxiliary response files (arf) by using the FTOOLS command *addarf*, using the weighting factor of each individual arf by dividing the individual exposure time of each single observation by the total exposure time of the merged spectrum.

The UV-optical telescope (UVOT; Roming et al. 2005) data of each segment were co-added in each filter with the UVOT task *wotimsum*. In general, all observations were performed in all 6 UVOT filters, except if the observation was interrupted by Gamma-Ray Burst detections or higher priority Target of Opportunity observations. Source counts in all 6 UVOT filters were

² https://www.swift.ac.uk/user_objects/

³ <https://www.swift.ac.uk/LSXPS/>

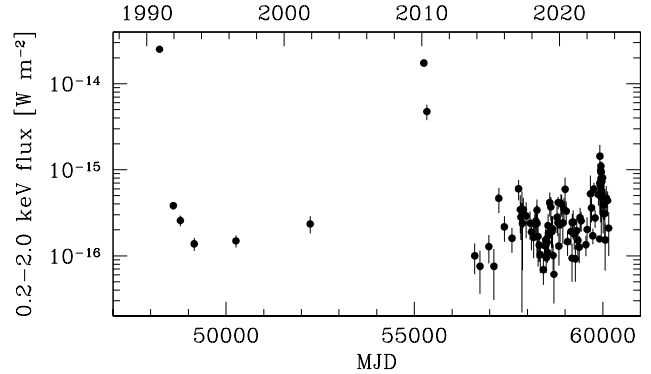


Figure 1. Long-term 0.2-2.0 keV X-ray light curve of IC 3599. The data during the 1990s are from ROSAT, the 2002 observation from Chandra, and all others after 2010 from Swift. Data are available at [10.5281/zenodo.10899673](https://zenodo.org/record/10899673)

selected in a circle with a radius of $5''$ and background counts in a nearby source free region with a radius of $20''$. UVOT magnitudes and fluxes were measured with the task *wotsource* based on the most recent UVOT calibration as described in Poole et al. (2008) and Breeveld et al. (2010). The UVOT data were corrected for Galactic reddening ($E_{B-V} = 0.015$; Schlegel et al. 1998). The correction factor in each filter was calculated with equation (2) in Roming et al. (2009) who used the standard reddening correction curves by Cardelli et al. (1989).

3. RESULTS

3.1. X-ray and UV/Optical Light Curves

3.1.1. Light Curves

The fluxes in X-rays and in the UV/optical obtained by *Swift* are listed in Table 3. This table also contains the observations published already in Grupe et al. (2015) which were re-analyzed due to updates in the calibration files. The full machine-readable table is available on Zenodo: [10.5281/zenodo.10899673](https://zenodo.org/record/10899673). Note that many 0.3-10 keV fluxes were estimated from the count rates derived from the Leicester *Swift*-XRT Product tool (see footnote 1) and then converted to fluxes based on the closest X-ray data that allowed a spectral analysis. These estimated fluxes are marked in Table 3.

Figure 1 displays the long-term X-ray light curve of IC 3599. The data for this light curve are available on Zenodo: [10.5281/zenodo.10899673](https://zenodo.org/record/10899673). The light curves clearly show the two giant outbursts seen by ROSAT and *Swift* about 20 years apart. The long-term light curve also displays a mini flare which shows an increase in X-ray flux by a factor of about 10 in December 2022.

Figure 2 displays the full *Swift* light curve between 2010 and August 2023. Note that due to the low background in the *Swift* XRT even a low number of counts

results in a 3σ detection. However, the number of counts is often too low to allow for a reliable determination of the hardness ratio. It displays the outburst in 2010 and the remarkable flat light curve since *Swift* resumed the observations with our monitoring program in 2013. The green vertical lines mark the year 2019 when [Campana et al. \(2015\)](#) predicted that the hypothetic star would return and undergo another partial disruption event while going through periastron and thus form a temporary accretion disk around the black hole again, causing another outburst. Clearly, this did not happen. There are no signs of unusual activity in X-rays or UV, yet. There is, however, a general trend since about 2021 that IC 3599 is slowly becoming brighter in X-rays (see below in [Section 3.1.3](#)). The hardness-ratio light curve suggests strong spectral variability in X-rays as well.

Figure 3 shows the *Swift* XRT and UVOT light curves from November 2022 to August 2023. It shows a very dense monitoring phase in January 2023 due to the unusually high count rate of $0.03 \text{ counts s}^{-1}$ seen in December 2022. This is a factor of 10 higher than typically observed when it is in its very low state (see also [Figure 2](#)). The light curve also displays a remarkable hardening of the X-ray spectrum after the mini flare from being very soft at almost $\text{HR}=-1$ to becoming harder with $\text{HR}>0$. However, from about March 2023 to the end of the observing campaign in August 2023, IC 3599 has become softer again.

3.1.2. Variability Analysis

We have monitored IC 3599 regularly since 2013 which has led to a total number of more than 100 observations. This rich data set allows for a detailed temporal analysis. As the first step we can apply the Fractional Excess Variance $F_{\text{var}} = \frac{\sqrt{\sigma^2 - \delta^2}}{\langle f \rangle}$ as defined by [Rodríguez-Pascual et al. \(1997\)](#) with an uncertainty of $\sigma_{F_{\text{var}}} = \frac{1}{F_{\text{var}}} \sqrt{\frac{1}{2N} \frac{\sigma^2}{\langle f \rangle^2}}$ following the definition by [Edelson et al. \(2002\)](#). Here, σ is the variance of the light curve, δ is the mean value of the uncertainties of the fluxes/count rates, and $\langle f \rangle$ is the mean value of the fluxes/count rates. We applied this to the *Swift* XRT and UVOT light curves including and excluding the 2010 outburst data. The results of the fractional excess variance are listed in [Table 1](#).

While the results of the fractional excess variance including the 2010 outburst data seem to follow the decrease of F_{var} with increasing wavelength as expected from accretion disc reprocessing models (e.g. [Cackett et al. 2007](#)), excluding these data shows a different picture: The same overall trend is still visible, however 2 bands (U and V) deviate from the systematic trend.

Table 1. Fractional excess variance and the mean fluxes $\langle f \rangle$ of the *Swift* XRT and UVOT light curves including all data and only the low state 2013-2023 data.

Band	All Data		2013-2022 low state	
	F_{var}	$\langle f \rangle$	F_{var}	$\langle f \rangle$
F_X	2.616 ± 0.159	3.911	0.759 ± 0.055	2.735
UVW2	0.140 ± 0.010	2.451	0.048 ± 0.006	2.415
UVM2	0.156 ± 0.011	2.531	0.037 ± 0.010	2.482
UVW1	0.131 ± 0.010	2.691	0.018 ± 0.013	2.656
U	0.112 ± 0.008	3.786	0.041 ± 0.006	3.741
B	0.042 ± 0.005	7.302	0.007 ± 0.015	7.276
V	0.119 ± 0.009	9.419	0.114 ± 0.008	9.373

When working with a variance and mean, the assumption is that the underlying distribution is Gaussian ([Gauß 1821](#)). We checked the flux distributions in X-rays and in each UVOT filter using R (e.g., [Crawley 2009](#)) by looking at the histogram of the flux distribution as well as at the quantile-quantile plot (QQ plot). We found that this assumption is well-justified for the UVOT observations. Except for the high state data from 2010, the data of all UVOT observations are well-described by a Gaussian distribution in all 6 filters. [Figure 4](#) displays the distribution and the QQ plot of the W2 magnitudes of IC 3599 which clearly shows that this is a Gaussian distribution. The other UVOT filters show similar distributions which are all consistent with a Gaussian distribution.

However, the X-ray flux variations are not represented by a Gaussian distribution. This is clearly shown in [Figure 5](#) which displays the histogram and the QQ-plot.

For non-Gaussian distributions, the variance and the mean are not good measures of a sample and in these cases, the median is a much better measure than the mean. In order to study the overall variability in all *Swift* XRT and UVOT light curves we designed a new measure: a variability parameter

$$P_{\text{var}} = \frac{1}{\sqrt{N}} \frac{1}{x_{\text{med}}} \sqrt{\sum_i (x_i - x_{\text{med}})^2 \times \frac{\delta_{\text{med}}^2}{\delta_i^2}} \quad (1)$$

which is like a reduced χ^2 value. This parameter, P_{var} , is a measure of how strongly a source deviates from the median value. Here x_{med} and δ_{med} are the sample median values of the fluxes and the median of the uncertainties. The values x_i and δ_i are the individual values with their uncertainties. The term $\frac{\delta_{\text{med}}^2}{\delta_i^2}$ is a weighing factor that takes the individual uncertainties into account so that values with large uncertainties carry less weight in the calculations than those values

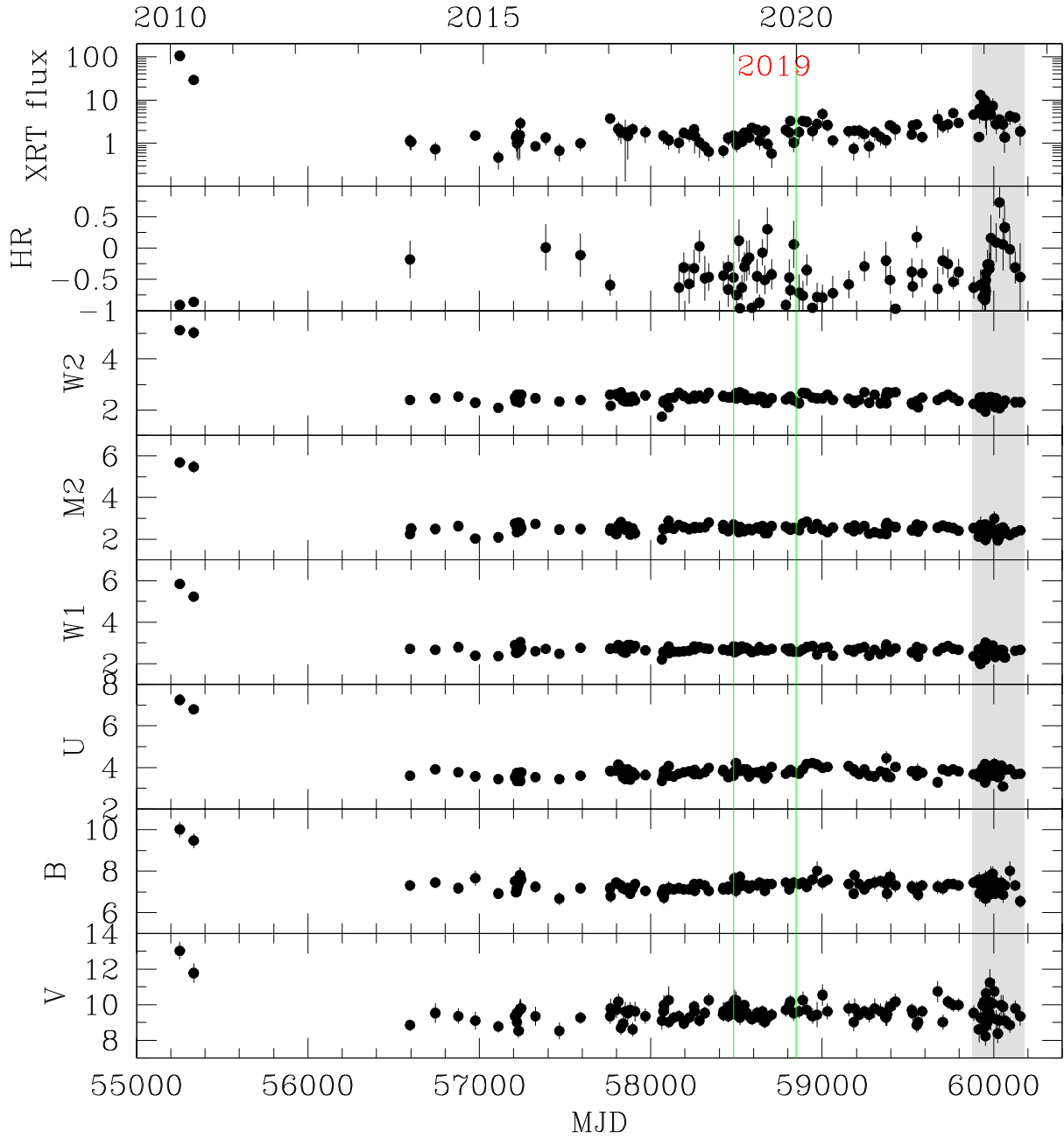


Figure 2. Observed Swift X-ray to optical light curve of IC 3599 from 2010 to August 2023. The fluxes in the X-ray and UVOT bands are given in units of $10^{-16} \text{ W m}^{-2}$. The grey-shaded area displays the range of the 2023 Swift light curve displayed in Figure 3.

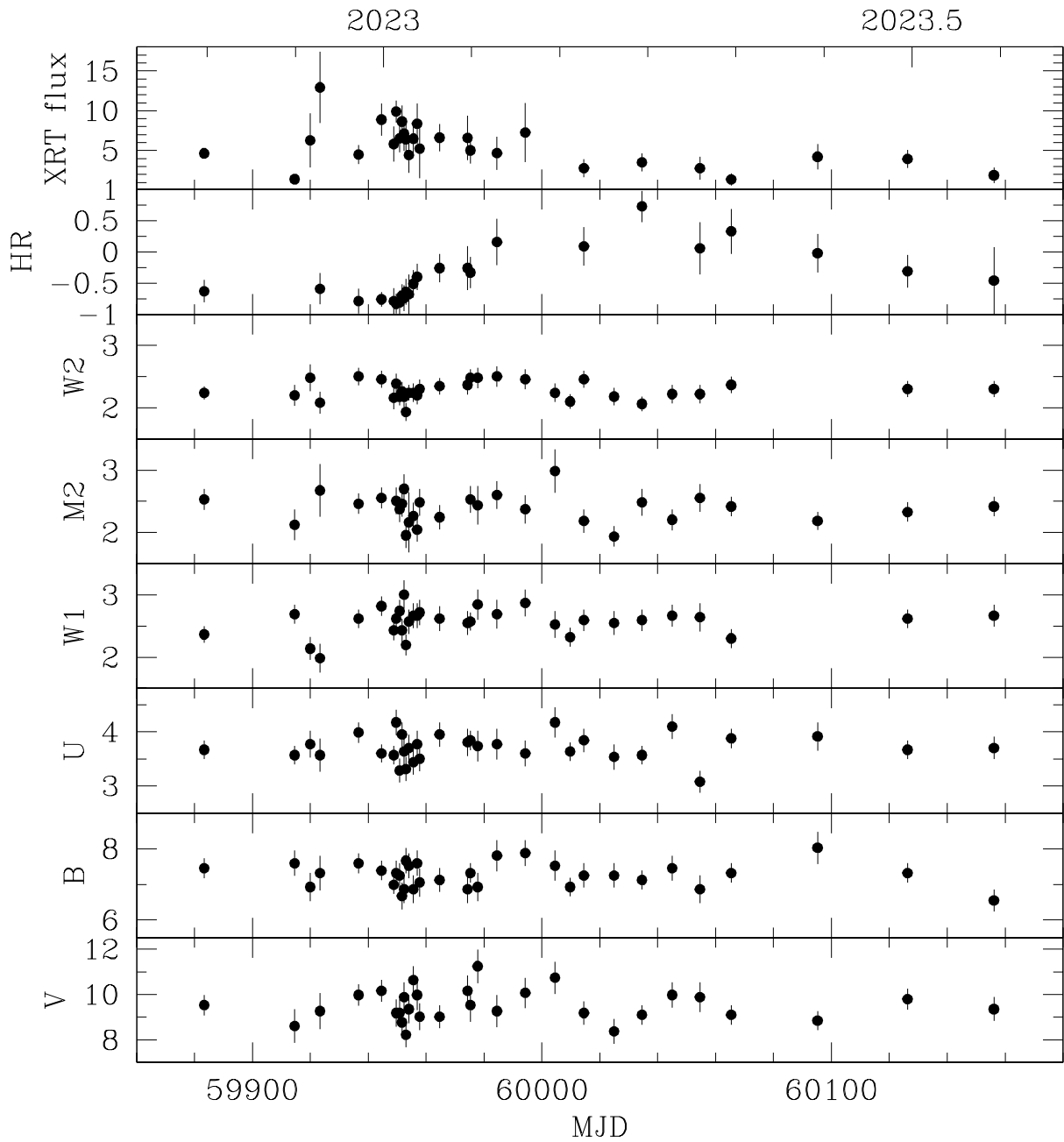


Figure 3. Observed Swift X-ray to optical light curve of IC 3599 from 2022 November to 2023 August. The fluxes in the X-ray and UVOT bands are given in units of $10^{-15} \text{ W m}^{-2}$.

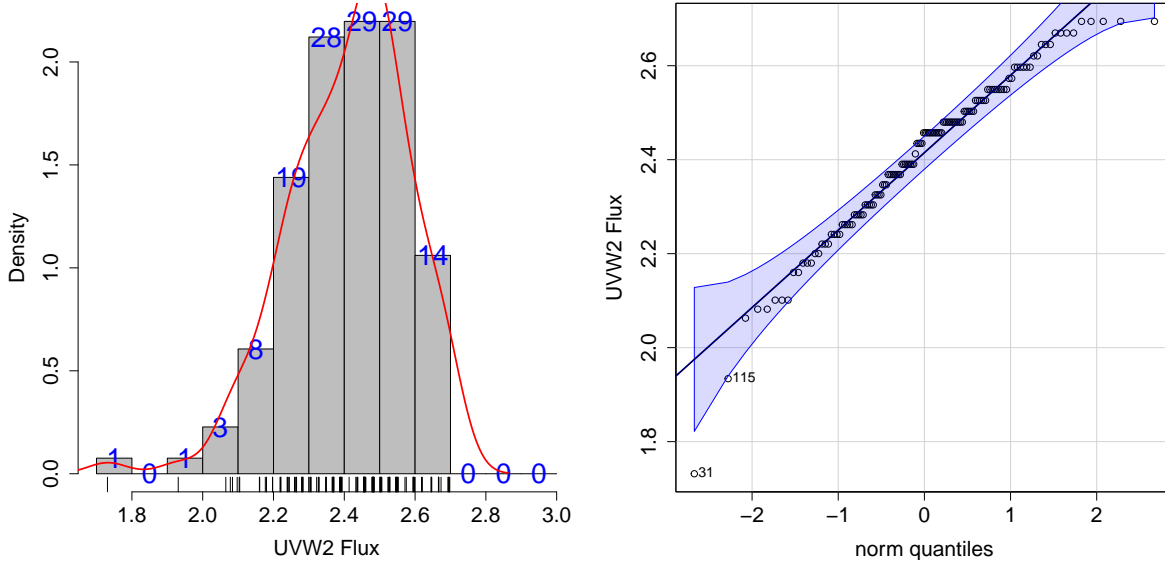


Figure 4. Histogram and QQ-Plot of the W2 fluxes of IC 3599 (in unites of $10^{-15}W m^{-2}$)

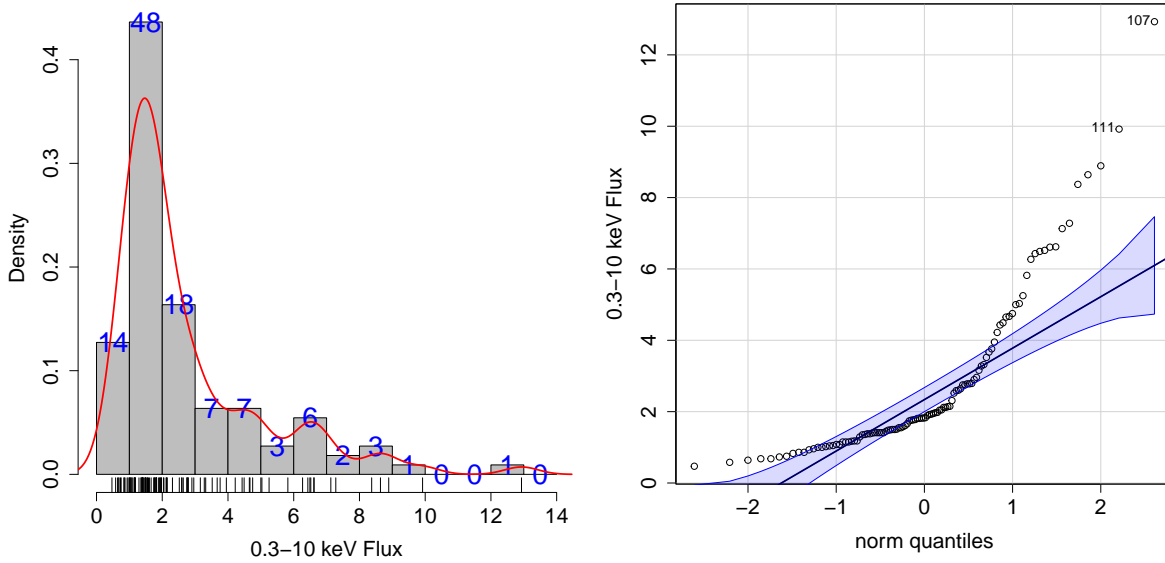


Figure 5. Histogram and QQ-Plot of the 0.3-10 keV X-ray fluxes of IC 3599 (in unites of $10^{-16}W m^{-2}$)

with small uncertainties. We estimate the uncertainties on the values of P_{var} by $\Delta P_{\text{var}} = \frac{\delta_{\text{med}}}{x_{\text{med}}} P_{\text{var}}$. The values for P_{var} are listed in Table 2. These values also confirm the stronger variability in X-rays than in the UV and optical. The variability parameter P_{var} also shows that these values are not dominated by the 2010 outburst measurements. It allows a direct comparison with the variability strength between Gaussian distributed data and non-Gaussian data, like the X-ray flux distribution of IC 3599, simply because it does not assume a Gaussian distribution and it is therefore a more general measure of the variability.

Just a Gaussian flux distribution by itself does not prove that these are just random fluctuations. In order to check on any variability we performed a periodogram within R using *spec.pgram*. Besides some red noise at lower frequencies, we only found white noise in the data. The V filter data are dominated by white noise. This variability pattern is typical for type 2 AGN (Wang et al. 2024) and may suggest that IC 3599 remains in its Seyfert 1.9 state at this time.

Table 2. Variability parameter P_{var} and the median flux f_{med} of the *Swift* XRT and UVOT light curves of the low state 2013-2023 data

band	all data		2013-2022 low state	
	P_{var}	f_{med}	P_{var}	f_{med}
F_X	1.072 ± 0.410	1.830	0.808 ± 0.306	1.820
UVW2	0.107 ± 0.006	2.457	0.073 ± 0.004	2.457
UVM2	0.112 ± 0.007	2.508	0.073 ± 0.005	2.508
UVW1	0.107 ± 0.006	2.667	0.059 ± 0.003	2.667
U	0.093 ± 0.004	3.772	0.060 ± 0.003	3.772
B	0.049 ± 0.002	7.318	0.039 ± 0.002	7.319
V	0.094 ± 0.005	9.529	0.088 ± 0.004	9.529

3.1.3. Merged XRT and UVOT Light Curves

Figure 6 displays the long-term *Swift* XRT light curve with the data averaged over each year, except for the 2013-2016 period because the number of observations is relatively small and the count rate was low, of the order of $0.003 \text{ counts s}^{-1}$. We binned the 2013-2015 and 2015-2017 observations into one bin each and after 2017, the observations of each year were combined. The binned data are displayed as red data points in Figure 6. The 0.3-10 keV fluxes and the hardness ratios for these periods are listed in Table 2. There is clearly an overall slow brightening in X-rays over the last decade. The hardness ratio light curve also suggests spectral variability with IC 3599 becoming softer from 2013 to 2020, but becoming harder again since. However, there is no correlation between the hardness ratio and the X-ray brightness of IC 3599.

Figure 7 displays the UVOT light curves between 2013 and 2023 with the merged data shown in red. Overall, there is no significant variability from year to year. The results for the merged data are listed in Table 4. Figure 7 and Table 4 show that there is no significant variability on long or short time scales, not even a trend like seen in X-rays. This is somewhat expected given the Gaussian distribution of the UVOT data.

3.2. X-ray Spectral Analysis

For the comparison of the high and low states we merged the 2010 February and May data into a high state spectrum and did the same for the low state by merging all data from 2013 to 2023. The high and low state data were then fitted with various spectral models. The results of these fits are listed in Table 3. All models were fitted with the $z=0$ absorption fixed to the Galactic value of $1.17 \times 10^{20} \text{ cm}^{-2}$.

The total exposure time of the high state spectrum was 3354s and the count rate $0.115 \text{ counts s}^{-1}$ which

means a total number of source counts of 260 counts which account for 99.3% of the counts in the spectrum. The relatively low number of counts in the high-state spectrum only allowed for an analysis using W statistics (Cash 1979).

The overall count rate of the low-state spectrum is $0.0046 \text{ counts s}^{-1}$ and has a total exposure time of 302 ks. This results in a total number of about 1400 source counts, which accounts for 89% of the counts in the spectrum. The relatively large number of counts allows us to fit the low-state spectrum with χ^2 statistics. The binning of the low-state spectrum was 20 counts per bin. This spectrum is displayed in Figure 8.

The high and low flux state spectra were first fitted by a single power law model. While in the high state case the data can be fitted by this model acceptably, the low state spectrum clearly deviates from a simple power law model as shown from the fit parameters in Table 3 and in Figure 8. One thing to keep in mind is that the number of counts in the high state data above 1.5 keV is so low that we do not have any information on the spectrum above this energy. Next, we applied a broken power law model and a blackbody plus power law model. These are phenomenological models that can describe the spectra quite well in both cases. Finally, we used a neutral partial covering absorber model. For the high state data, the parameters of the partial covering absorber are unconstrained. There are no data at higher energies that are needed to fit this model. For the low state data however, the spectrum is well described by a partial covering absorber model with a column density of $6 \times 10^{22} \text{ cm}^{-2}$ and a covering fraction of 80%.

Figure 9 displays an absorbed blackbody plus power law model fit to the merged high state data from 2010 and the 2013-2022 low state data. Note, that for display purposes the high state data have been binned, however the spectral fits were performed with unbinned data using W-statistics (Cash 1979). The blackbody component is displayed in red while the power law component is shown in green. As for the change between the high and low state black body and power law components, the black body component changes by a factor of 48 ± 13 and the power law component by a factor of 23 ± 6 . This suggests that the blackbody component decreased stronger than the power law component.

3.3. Strong X-ray Spectral Change in January 2023

As shown in the hardness ratio light curve in Figure 3 there is a strong spectral change from being a very soft source to a significantly harder AGN around MJD 59954-59977 (2023-January-10 to 31). In order to study the change in the X-ray spectrum, we merged

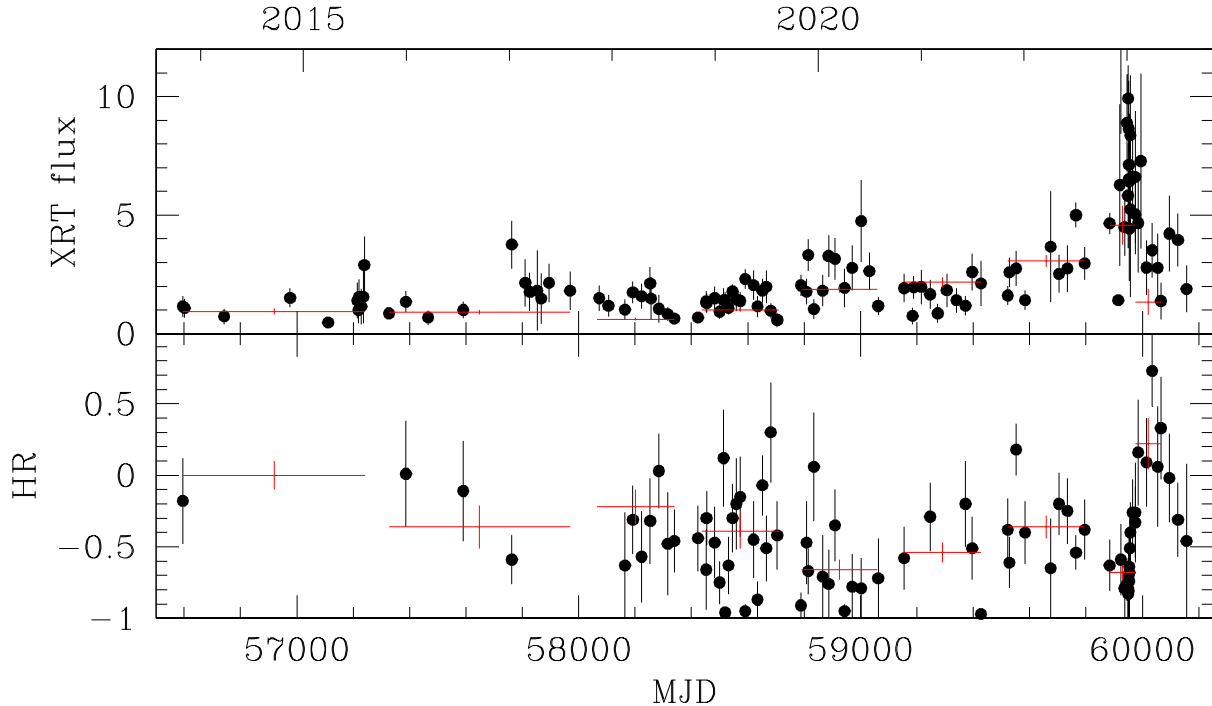


Figure 6. Swift XRT 0.3-10 keV flux (in units of $10^{-16} \text{ W m}^{-2}$) and hardness ratio long-term light curves. The black data points displayed in Figure 2 show detections. The red data points display merged data.

the data after IC 3599 emerged from its sun constraint on 2022-October-31 to 2023-January-10 when it was in the soft state and between 2023-February-10 and May-01 when it was in the hard state. Both spectra can be fitted by simple power law models. For the soft and hard phases, the photon indices were $\Gamma = 4.03^{+0.37}_{-0.33}$ and $\Gamma = 1.70^{+0.87}_{-0.54}$, respectively. During the soft state the AGN is also brighter with a flux of $F_{0.3-10\text{keV}} = (4.33 \pm 0.40) \times 10^{-16} \text{ W m}^{-2}$, while during the hard state the flux was at $(1.34 \pm 0.58) \times 10^{-16} \text{ W m}^{-2}$. Since about March 2023 IC 3599 has transitioned again into a softer X-ray state.

3.4. UV Morphology

Figure 10 displays the W2 image which was merged from all low-state W2 data from 2013-2023. This image has a total exposure time of 99 ks. The image clearly shows the spiral structure of the host galaxy, tracing the young, blue, stars in the spiral arms. The projected angular diameter of the galaxy is about $75''$ which corresponds to a physical size of 33 kpc; larger than a typical dwarf galaxy, suggesting that the SMBH mass of IC 3599 is not particularly low.

3.5. UV Colors

Although the Gaussian distributions of the magnitudes in all 6 UVOT filters during the low state suggest random fluctuations, we still checked if there may be any dependence on the colors with fluxes in X-rays and the UV. For this purpose, we calculated U-B and W2-W1 colors and correlated them with various properties, like W2 magnitude, count rate and hardness ratio. As expected, we did not find any correlations among these parameters.

3.6. Spectral Energy Distribution

The Spectral Energy Distribution (SED) of IC 3599 during the February 2010 outburst and the 2013-2023 low state is shown in Figure 11. It displays how dramatically different the SED of IC 3599 was during the 2010 outburst. The optical/UV to X-ray spectral slope α_{ox} ⁴ during the outburst was $\alpha_{\text{ox}} = 1.57 \pm 0.07$ and during the low state $\alpha_{\text{ox}} = 1.79 \pm 0.04$. Note that the uncertainties on the α_{ox} value during the outburst maybe larger, be-

⁴ The optical/UV to X-ray spectral slope α_{ox} is defined by Tananbaum et al. (1979) as $\alpha_{\text{ox}} = -0.384 \times (\log(l_{2\text{keV}}) - \log(l_{2500\text{\AA}}))$, where $l_{2500\text{\AA}}$ and $l_{2\text{keV}}$ are the luminosity densities at 2500 Å and 2 keV.

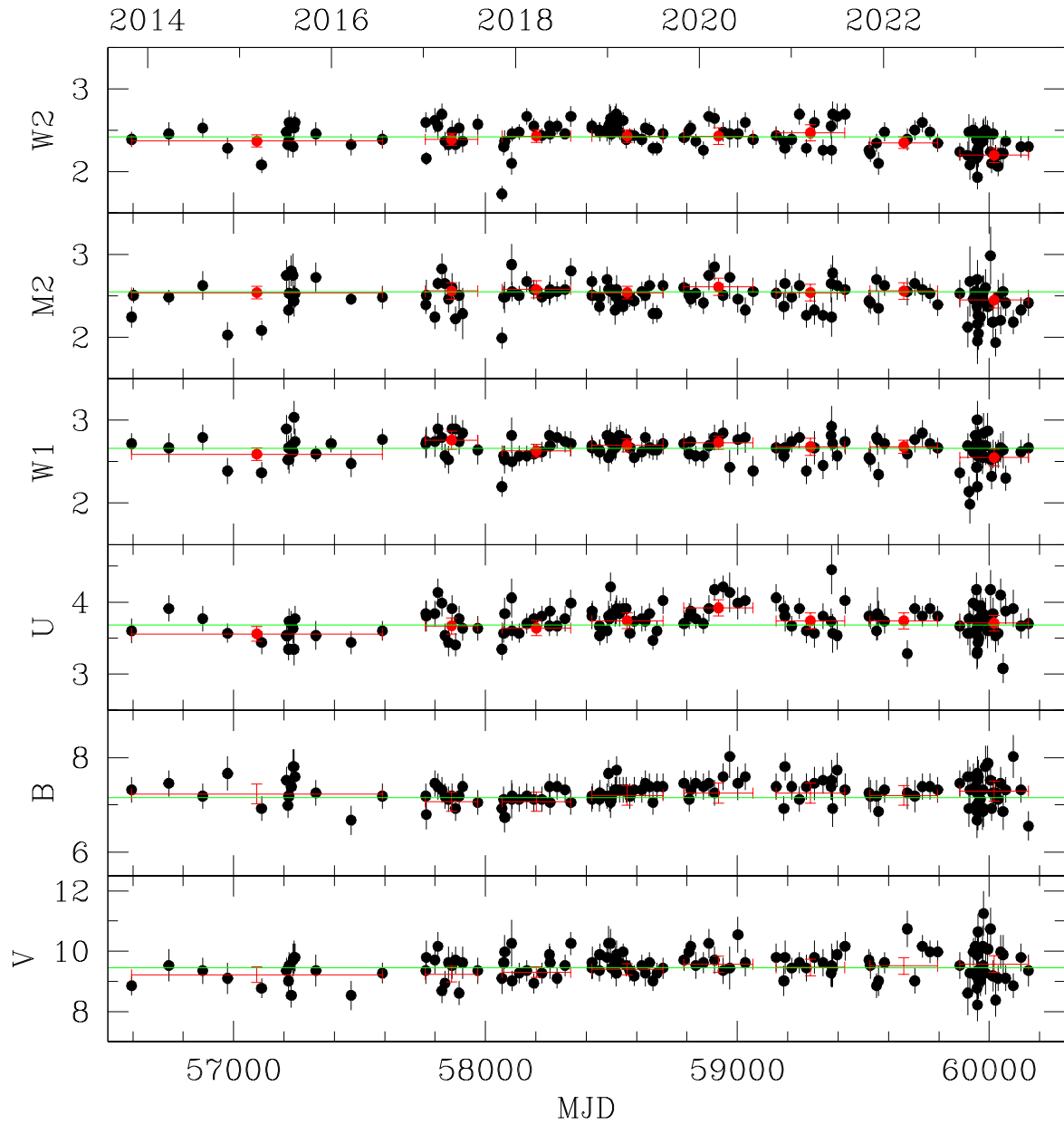


Figure 7. Swift UVOT long-term light curves. The fluxes are given in units of $10^{-15} \text{ W m}^{-2}$. The black data points display as in Figure 2 each observation with a detection. The red data points display merged data as listed in Table 4. The vertical green lines mark the median values in each of the filters.

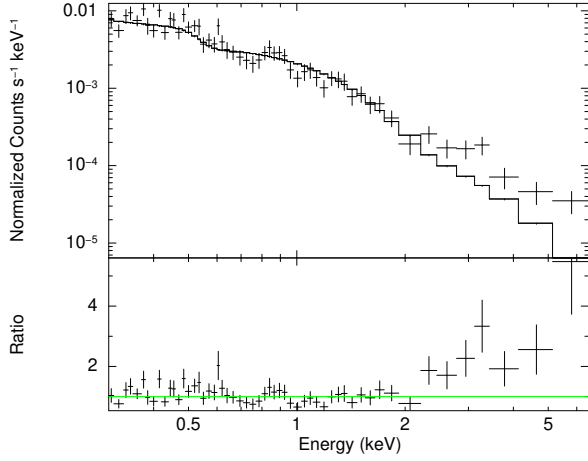


Figure 8. Upper panel: Swift XRT spectrum of all low state 2013-2023 data merged fitted by an absorbed single power law model. Lower panel: The ratio between the data and the model.

Table 3. Spectral analysis of the high and low state XRT spectra. The high state data were fitted with W statistics, while for the low state data, χ^2 statistics was applied.

Parameter	2010 High	2013-2023 Low
powerlaw		
Γ	4.32 ± 0.20	3.12 ± 0.10
χ^2/ν	111/82	87.9/53
broken power law		
Γ_1	3.51 ± 0.40	3.29 ± 0.15
E_{break} [keV]	0.85 ± 0.13	$1.53^{+0.62}_{-0.38}$
Γ_2	7.30 ± 1.50	$1.96^{+0.43}_{-0.67}$
χ^2/ν	76/82	61.3/51
blackbody + power law		
kT [eV]	112 ± 12	95 ± 9
Γ	4.56 ± 1.65	2.18 ± 0.26
F_{bb} [W m^{-2}]	3.8×10^{-15}	7.5×10^{-17}
F_{po} [W m^{-2}]	2.0×10^{-15}	9.6×10^{-17}
χ^2/ν	76/82	57.9/51
xpcfabs \times power law		
N_H^1	6.30^2	$6.30^{+4.62}_{-2.51}$
f_{pc}	0.05^3	$0.80^{+0.07}_{-0.11}$
Γ	4.32 ± 0.20	3.27 ± 0.12
χ^2/ν	111/82	60.1/51

¹ The redshifted ($z=0.021$) partial covering absorber column density is given in units of 10^{22}cm^{-2} . ² The partial covering absorber column density is fixed to $6.3 \times 10^{22} \text{cm}^{-2}$. ³ not constraint

cause to determine the 2 keV data point we assumed a simple power law model, which may not be the correct model at 2 keV, but with the lack of available data it is the value derived from the X-ray spectral fit.

For the 2010 outburst data and applying the simple power law model, we derived a 0.2-2.0 keV luminosity of $L_X = (9.9 \pm 0.8) \times 10^{35} \text{W}$. Applying the relation $\log L_{\text{bol}} = 1.23 \times \log(L_X) - 7.36$ as given in Grupe et al. (2010) we estimated the bolometric luminosity as $8 \times 10^{36} \text{W}$. Assuming a black hole mass of IC 3599 of $2.5 \times 10^6 M_\odot$ the Eddington luminosity is $3.15 \times 10^{37} \text{W}$ which then results in an Eddington ratio of $L/L_{\text{Edd}} = 0.25$.

As for the low state 2013-2023 data, assuming the broken power law model as shown in Table 3, the 0.2 - 2.0 keV luminosity is $1.8 \times 10^{34} \text{W}$ which results in a bolometric luminosity of $6 \times 10^{34} \text{W}$ and an Eddington ratio of $L/L_{\text{Edd}} = 2 \times 10^{-3}$.

In addition, the SED (Figure 11) also displays the SED of the data during the December 2022 flare period (open magenta circles) and the data after the mini flare from February to May 2023 (open green triangles). Note that for visualization purposes we have binned the data with a binning of 10. For the spectral fits, no binned data were used applying W statistics (Cash 1979). The X-ray data after the mini flare indicate a significant flux increase in the hard X-ray band. The spectral analysis of these data results in a very flat X-ray spectrum with $\Gamma = 1.70^{+0.81}_{-0.51}$, significantly flatter than what has been observed during the entire 2013-2022 low state period. Note that the low number of counts did not allow for a more sophisticated spectral analysis.

4. DISCUSSION

4.1. High-Amplitude Variability of AGN

In principle, any single one of a huge number of small or large flares in any blazar or radio-quiet AGN could be a TDE. However, TDEs are very rare events, and almost every single AGN or blazar is known to vary (see Ulrich et al. 1997; Gaskell 2008; Gallo 2018, for reviews). Therefore, exceptional positive evidence is required for any claim of a TDE in an AGN, as emphasized by, e.g., Rees (1988) and Komossa & Bade (1999). The situation is completely different, when a *quiescent* galaxy suddenly shows a huge X-ray outburst, because the only known model to explain a quasar-luminosity outburst in a galaxy without long-lived accretion disk is a TDE. IC 3599 is a bona fide AGN with a long-lived NLR (Komossa & Bade 1999; Grupe et al. 2015), and closely resembles the increasing number of changing-look AGN identified in recent years (e.g. Alloin et al. 1986; Runco

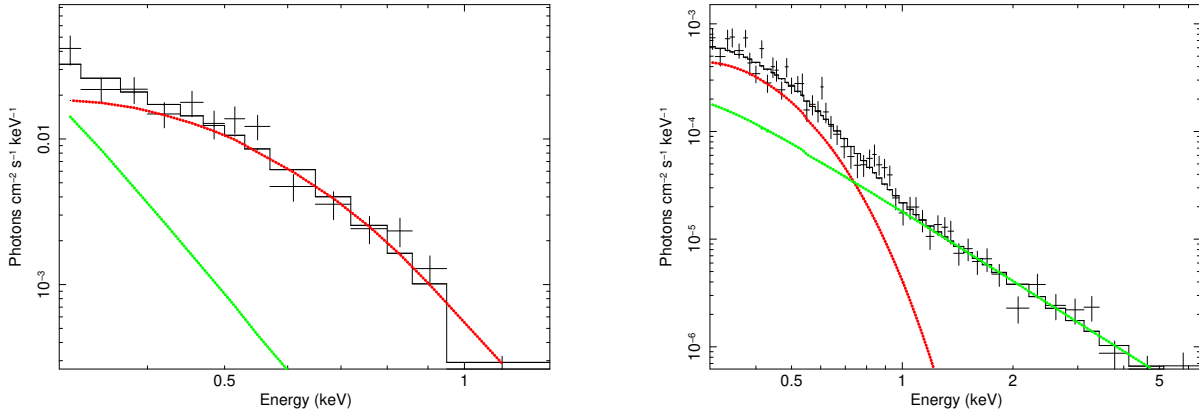


Figure 9. Swift XRT merged high and low state spectra (left and right, respectively) The red line displays the black body spectrum and the green line, the power law component.

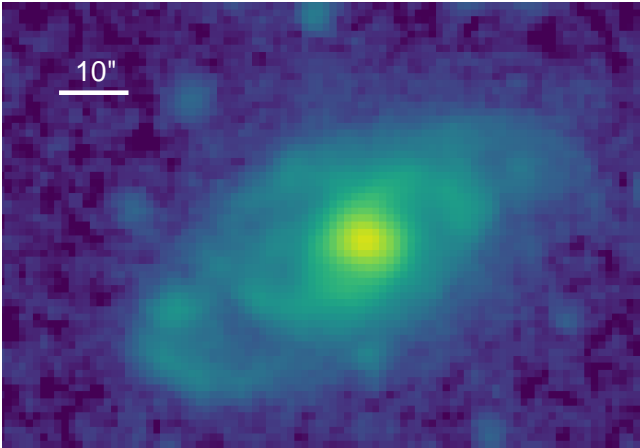


Figure 10. Swift UVOT W2 image of IC 3599. At the distance of IC 3599, $10''$ corresponds to 4.4 kpc.

et al. 2016; MacLeod et al. 2019; Frederick et al. 2019; Ochmann et al. 2024).

Therefore, so far, no definite positive evidence for a rare TDE in this highly variable AGN has been presented. However, we note that Mandel & Levin (2015) mentioned in passing the possibility of tidal disruption of one star and later tidal stripping of the second star of a binary star system in context of IC 3599. In that case, the near-identical peak luminosities of the two outbursts of IC 3599 would be unexpected. Further, w.r.t. the two outbursts of IC 3599, Komossa et al. (2014) pointed out that during certain phases of binary SMBH evolution, or in the presence of a recoiling SMBH, TDE rates can be temporarily strongly enhanced (Chen et al. 2009; Komossa & Merritt 2008; Stone & Loeb 2011), but two events within decades would still be rare, and IC 3599 does not show evidence for a recent major merger (e.g., Figure 10), and the near-identical peak luminosities of

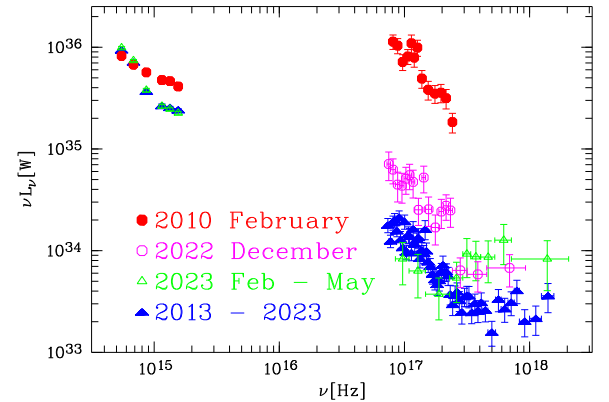


Figure 11. The SED of IC 3599 between the outburst in February 2010 (red), the merged 2013-2023 low state data (blue), the mini flare data in December 2022 (magenta), and the merged data after the mini flare (green). Note that the UVOT data during this flare are not shown due to their similarity to the overall low-state data.

the two outbursts would have to be coincidence. Therefore, Komossa et al. (2014) re-emphasized that TDEs are most reliably identified in quiescent galaxies. Further, Grupe et al. (2015) commented on the TDE model of Liu et al. (2009) (see also Liu et al. 2014) in application to IC 3599. Liu et al. (2009) predicted TDE light curves for stellar disruption in a binary SMBH system, showing characteristic recurrent flare and dip events. However,

the timing and amplitudes of IC 3599 did not fit that model.⁵

The one TDE model with explicit predictions which we can now test and rule out with the new monitoring data presented here, is the published repeat-tidal-stripping scenario for IC 3599, because that model made testable predictions for the time frame covered in our new observations. We come back to this model in the following paragraphs. Beyond that, we continue to consider AGN scenarios, rather than TDE scenarios, for this highly variable AGN. Below, we also discuss the other aspects of the long-term variability of IC 3599, unrelated to the two big outbursts.

4.2. No Outburst of IC 3599 in 2019/2020

Campana et al. (2015) predicted that there would be another outburst due to the partial tidal stripping of an orbiting star in 2019 and 2020. They predicted a 9.5 year period. The model also assumed a black hole mass of the order of a few $10^5 M_\odot$. While in general a TDE scenario cannot be excluded in principle, as pointed out by Grupe et al. (2015) and Komossa & Bade (1999), IC 3599 is an AGN and the dramatic flaring in IC 3599 does not have to be associated with a tidal disruption event and that given the black hole mass estimates of IC 3599 of the order of several millions of solar masses, an accretion disk instability scenario would be more likely. Campana et al. (2015)'s prediction of repeat flaring made it possible to test the tidal stripping scenario. The *Swift* monitoring programs from 2019 and 2020 initiated by us and Campana clearly show that there is no outburst seen during this period (see Figure 2). This result clearly favors the accretion disk scenario as suggested by Grupe et al. (2015).

4.3. Slow Increase in X-ray Flux

Figure 6 suggests that there has been a slow overall increase in X-ray flux since about 2018. In the accretion disk scenario that could be explained by a slow fill-up of the inner part of the accretion disk which emptied out during the last outburst in 2010. In Grupe et al. (2015) we estimated the fill-up time to be several decades, following the relation $\tau_{\text{fill}} = 0.33\alpha^{-8/10} M_6^{6/5} \dot{M}_{\text{edd}}^{-3/10} (R_{\text{trunc}}^{5/4} - R_0^{5/4})$ given in units of month following the relation by Saxton et al. (2015). The other parameters are the viscosity α for which we assumed a standard value of 0.1, the black hole mass M_6

in units of $10^6 M_\odot$, the infill rate \dot{M}_{edd} in units of the Eddington limit. The truncation radius R_{trunc} and the inner radius R_0 are given in units of the gravitational radius $R_g = \frac{GM}{c^2}$.

While the X-ray flux seems to develop some long-term trend to become slightly brighter, there is no sign of any significant variability in the optical and UV. IC 3599 seems to be fairly constant in all 6 UVOT filters and the fluctuations seem to be random, which is supported by the Gaussian distributions of the magnitudes seen in each filter.

4.4. X-ray Mini Flare and Spectral Hardening Event in 2022/2023

As shown in Figure 6, there is an X-ray mini flare at the beginning of December 2022. Right after this short-lasting flare we see a dramatic hardening of the X-ray spectrum, as shown in the hardness ratio light curve in Figure 6. This hardening of the spectrum can also be seen in the spectral energy distribution in Figure 11. The data from this hardening event as displayed as green open triangles.

The mini flare started on 2022 December 01 and peaked on December 10 with a peak flux of $1.29 \pm 0.45 \times 10^{-15} \text{ W m}^{-2}$, which is a factor of about 10 higher than the flux on December 01 (see also Table 3). While the spectrum was very soft during the flare, the onset of the spectral hardening started around 2023 January 03 and reached the hardest state with a hardness ratio of 0.73 ± 0.25 on March 31. The spectrum became soft again by the end of May 2023 and has remained soft in all observations after that.

The question is raised, which physical process(es) cause this temporary spectral hardening. The hard X-ray spectral component, typically observed in all AGN, is usually interpreted as the presence of an accretion-disk corona. It is therefore possible that a corona formed temporarily, following the mini flare, and disappeared again in the low-state. Alternatively, we might speculate that a temporary absorption event caused an apparent spectral hardening. For instance, it is possible that due to the flaring activity a temporary outflow was triggered because of the increase in the accretion luminosity (Takeuchi et al. 2013). When a clumpy outflow partially covers the intrinsic emission, a spectral hardening can result. However, even at the peak of the mini flare, L/L_{Edd} is only about 0.02, whereas launching of radiation-pressure driven outflows requires values closer to 1.

The Swift snapshot observations do not contain enough photon statistics to distinguish between these different spectral models (like emission from a tempo-

⁵ Even though not discussed further here, we note that multiple outburst events in *quiescent* galaxies have been interpreted as possible partial stripping events; for example the case of RXJ133157.6324319.7 (Hampel et al. 2022) which showed a second outburst (Malyali et al. 2023) ~ 30 yrs after the first.

rary corona, versus partial covering absorption, or more complex spectral models involving the interplay of several components). Deeper, triggered, follow-up observations during the flare decline phase will be very useful, if new mini flares are detected in the future.

4.5. Black Hole Mass Estimates

While the repeating TDE model of Campana et al. (2015) requires a small black hole mass of a few $10^5 M_{\odot}$, all observational parameters, like the width of the [OIII] λ 5007 line, suggest a black hole mass that is at least 10 times larger (see our discussion in Grupe et al. (2015), where we also used BLR line width). The large physical size of IC 3599 as shown in Figure 10 may support a larger black hole mass as well, but the previous SMBH mass estimates using the various scaling relations are the most restrictive.

4.6. Conclusions

Despite the speculation in 1995 by Brandt et al. (1995) and Grupe et al. (1995), and the repeated-TDE model by Campana et al. (2015) that the X-ray outburst seen during the RASS could have been caused by a TDE, our long-term *Swift* monitoring campaign suggests otherwise, since the third outburst predicted by the repeat-TDE model in 2019/2020 did not happen. The X-ray outbursts seen in 1990 by ROSAT and 2010 by *Swift* are most likely caused by an accretion disk instability as favored by Grupe et al. (2015), since IC 3599 is not a quiescent galaxy but a bona fide AGN. In fact, IC 3599 is an extreme case of an optical changing-look AGN (Kommossa & Grupe 2023; Xu et al. 2024).

Independent of the nature of the big outbursts or their absence in 2019/2020 in particular, we have also studied the long-term X-ray flux and spectral variability properties of IC 3599 during its more quiescent levels. IC 3599 turns out to be highly variable in the X-ray regime. One event stood out: We found that IC 3599 exhibited an increase in its X-ray flux by a factor of about 10 in December 2022. This mini flare was followed by a remarkable hardening of the X-ray spectrum in the following months. One possible explanation for such a behavior could be the temporary formation of an accretion disk corona.

We will continue to monitor IC 3599 with *Swift*. It depends on the model, if and when a new outburst is expected. For instance, if the previous two outbursts were powered by a disk instability, it would depend on the

evolving and variable AGN disk properties, if and when a new instability occurs (note that the X-ray emission of IC 3599 in low-state is not constant but still varies, as in the majority of AGN). If, instead, there was an underlying strictly periodic process behind the outbursts, like variants of binary SMBH models where for instance a secondary SMBH interacts with the primary's disk once during its orbit, or binary SMBH models where stream-feeding from a circum-binary disk occurs, then the next outburst is expected around the year 2030. In case IC 3599 will exhibit another X-ray outburst again, we have a pre-approved ToO program with XMM that would allow us to study the inner-most environment of the central black hole.

1 We would like to thank *Swift* PI Brad Cenko for approv-
 2 ing our continued requests to observe IC 3599 and the
 3 *Swift* Science Operations team for executing the obser-
 4 vations. We would also like to thank the anonymous
 5 referee for useful comments and suggestions. This re-
 6 search has made use of the NASA/IPAC Extragalactic
 7 Database (NED) which is operated by the Jet Propul-
 8 sion Laboratory, Caltech, under contract with the Na-
 9 tional Aeronautics and Space Administration. This
 10 work made use of data supplied by the UK Swift Sci-
 11 ence Data Centre at the University of Leicester (Evans
 12 et al. 2007). This research has made use of the
 13 XRT Data Analysis Software (XRTDAS) developed un-
 14 der the responsibility of the ASI Science Data Center
 15 (ASDC), Italy. This research has made use of data ob-
 16 tained through the High Energy Astrophysics Science
 17 Archive Research Center Online Service, provided by
 18 the NASA/Goddard Space Flight Center.

Facilities: NASA Neil Gehrels Swift observatory (XRT and UVOT).

Software: HEASoft (<https://heasarc.gsfc.nasa.gov/docs/software/heasoft/>) with XSPEC (Arnaud 1996), ESO-MIDAS (<https://www.eso.org/sci/software/esomidas/>), the R programming language (<https://www.r-project.org/>), and SuperMongo (<https://www.astro.princeton.edu/~rhl/sm/>).

5. DATA AVAILABILITY

The raw *Swift* data of our project are available in the *Swift* archive at <https://swift.gsfc.nasa.gov/archive/>. The reduced results are available at Zenodo: [10.5281/zenodo.10899673](https://doi.org/10.5281/zenodo.10899673).

REFERENCES

- Alloin, D., Pelat, D., Phillips, M., & Whittle, M. 1985, The Astrophysical Journal, 288, 205, doi: [10.1086/162783](https://doi.org/10.1086/162783)
- Alloin, D., Pelat, D., Phillips, M. M., Fosbury, R. A. E., & Freeman, K. 1986, The Astrophysical Journal, 308, 23, doi: [10.1086/164475](https://doi.org/10.1086/164475)

- Arnaud, K. A. 1996, in *Astronomical Society of the Pacific Conference Series*, Vol. 101, *Astronomical Data Analysis Software and Systems V*, ed. G. H. Jacoby & J. Barnes, 17
- Bade, N., Komossa, S., & Dahlem, M. 1996, *Astronomy & Astrophysics*, 309, L35
- Bloom, J. S., Giannios, D., Metzger, B. D., et al. 2011, *Science*, 333, 203, doi: [10.1126/science.1207150](https://doi.org/10.1126/science.1207150)
- Brandt, W. N., Pounds, K. A., & Fink, H. 1995, *Monthly Notices of the Royal Astronomical Society*, 273, L47, doi: [10.1093/mnras/273.1.L47](https://doi.org/10.1093/mnras/273.1.L47)
- Breeveld, A. A., Curran, P. A., Hoversten, E. A., et al. 2010, *MNRAS*, 406, 1687, doi: [10.1111/j.1365-2966.2010.16832.x](https://doi.org/10.1111/j.1365-2966.2010.16832.x)
- Burrows, D. N., Hill, J. E., Nousek, J. A., et al. 2005, *Space Science Reviews*, 120, 165, doi: [10.1007/s11214-005-5097-2](https://doi.org/10.1007/s11214-005-5097-2)
- Burrows, D. N., Kennea, J. A., Ghisellini, G., et al. 2011, *Nature*, 476, 421, doi: [10.1038/nature10374](https://doi.org/10.1038/nature10374)
- Cackett, E. M., Horne, K., & Winkler, H. 2007, *MNRAS*, 380, 669, doi: [10.1111/j.1365-2966.2007.12098.x](https://doi.org/10.1111/j.1365-2966.2007.12098.x)
- Campana, S., Mainetti, D., Colpi, M., et al. 2015, *A&A*, 581, A17, doi: [10.1051/0004-6361/201525965](https://doi.org/10.1051/0004-6361/201525965)
- Cao, X., You, B., & Wei, X. 2023, *Monthly Notices of the Royal Astronomical Society*, 526, 2331, doi: [10.1093/mnras/stad2877](https://doi.org/10.1093/mnras/stad2877)
- Cardelli, J. A., Clayton, G. C., & Mathis, J. S. 1989, *The Astrophysical Journal*, 345, 245, doi: [10.1086/167900](https://doi.org/10.1086/167900)
- Cash, W. 1979, *ApJ*, 228, 939, doi: [10.1086/156922](https://doi.org/10.1086/156922)
- Chen, X., Madau, P., Sesana, A., & Liu, F. K. 2009, *ApJL*, 697, L149, doi: [10.1088/0004-637X/697/2/L149](https://doi.org/10.1088/0004-637X/697/2/L149)
- Craweley, M. 2009, *The R-Book*, John Wiley & Sons, Chichester, England
- Dexter, J., & Begelman, M. C. 2019, *Monthly Notices of the Royal Astronomical Society*, 483, L17, doi: [10.1093/mnrasl/sly213](https://doi.org/10.1093/mnrasl/sly213)
- Edelson, R., Turner, T. J., Pounds, K., et al. 2002, *ApJ*, 568, 610, doi: [10.1086/323779](https://doi.org/10.1086/323779)
- Evans, P. A., Page, K. L., Beardmore, A. P., et al. 2023, *MNRAS*, 518, 174, doi: [10.1093/mnras/stac2937](https://doi.org/10.1093/mnras/stac2937)
- Evans, P. A., Beardmore, A. P., Page, K. L., et al. 2007, *A&A*, 469, 379, doi: [10.1051/0004-6361:20077530](https://doi.org/10.1051/0004-6361:20077530)
- Frederick, S., Gezari, S., Graham, M. J., et al. 2019, *ApJ*, 883, 31, doi: [10.3847/1538-4357/ab3a38](https://doi.org/10.3847/1538-4357/ab3a38)
- Gallo, L. 2018, in *Revisiting Narrow-Line Seyfert 1 Galaxies and their Place in the Universe*, 34, doi: [10.22323/1.328.0034](https://doi.org/10.22323/1.328.0034)
- Gaskell, C. M. 2008, in *Revista Mexicana de Astronomia y Astrofisica Conference Series*, Vol. 32, *Revista Mexicana de Astronomia y Astrofisica Conference Series*, 1–11, doi: [10.48550/arXiv.0711.2113](https://doi.org/10.48550/arXiv.0711.2113)
- Gauß, C. 1821, *Commentationes Societatis Regiae Scientiarum Gottingensis Recentiores. Comm. Class. Math.*, 5, 33
- Gehrels, N., Chincarini, G., Giommi, P., et al. 2004, *The Astrophysical Journal*, 611, 1005, doi: [10.1086/422091](https://doi.org/10.1086/422091)
- Gezari, S., Martin, D. C., Milliard, B., et al. 2006, *ApJL*, 653, L25, doi: [10.1086/509918](https://doi.org/10.1086/509918)
- Grupe, D., Beuermann, K., Mannheim, K., et al. 1995, *A&A*, 299, L5, doi: [10.48550/arXiv.astro-ph/9505085](https://doi.org/10.48550/arXiv.astro-ph/9505085)
- Grupe, D., Beuermann, K., Mannheim, K., & Thomas, H. C. 1999, *Astronomy & Astrophysics*, 350, 805, doi: [10.48550/arXiv.astro-ph/9908347](https://doi.org/10.48550/arXiv.astro-ph/9908347)
- Grupe, D., Komossa, S., Leighly, K. M., & Page, K. L. 2010, *The Astrophysical Journal Supplement Series*, 187, 64, doi: [10.1088/0067-0049/187/1/64](https://doi.org/10.1088/0067-0049/187/1/64)
- Grupe, D., Komossa, S., & Saxton, R. 2015, *ApJL*, 803, L28, doi: [10.1088/2041-8205/803/2/L28](https://doi.org/10.1088/2041-8205/803/2/L28)
- Hampel, J., Komossa, S., Greiner, J., et al. 2022, *Research in Astronomy and Astrophysics*, 22, 055004, doi: [10.1088/1674-4527/ac5800](https://doi.org/10.1088/1674-4527/ac5800)
- Hill, J. E., Angelini, L., Morris, D. C., et al. 2005, in *Society of Photo-Optical Instrumentation Engineers (SPIE) Conference Series*, Vol. 5898, *UV, X-Ray, and Gamma-Ray Space Instrumentation for Astronomy XIV*, ed. O. H. W. Siegmund, 325–340, doi: [10.1117/12.618026](https://doi.org/10.1117/12.618026)
- Kaaz, N., Liska, M. T. P., Jacquemin-Ide, J., et al. 2023, *The Astrophysical Journal*, 955, 72, doi: [10.3847/1538-4357/ace051](https://doi.org/10.3847/1538-4357/ace051)
- Komossa, S. 2015, *Journal of High Energy Astrophysics*, 7, 148, doi: [10.1016/j.jheap.2015.04.006](https://doi.org/10.1016/j.jheap.2015.04.006)
- Komossa, S., & Bade, N. 1999, *Astronomy & Astrophysics*, 343, 775. <https://arxiv.org/abs/astro-ph/9901141>
- Komossa, S., & Greiner, J. 1999, *Astronomy & Astrophysics*, 349, L45. <https://arxiv.org/abs/astro-ph/9908216>
- Komossa, S., & Grupe, D. 2023, *Astronomische Nachrichten*, 344, e20230015, doi: [10.1002/asna.20230015](https://doi.org/10.1002/asna.20230015)
- Komossa, S., Grupe, D., Saxton, R., & Gallo, L. 2014, in *Proceedings of Swift: 10 Years of Discovery (SWIFT 10)*, 143, doi: [10.22323/1.233.0143](https://doi.org/10.22323/1.233.0143)
- Komossa, S., & Merritt, D. 2008, *ApJL*, 683, L21, doi: [10.1086/591420](https://doi.org/10.1086/591420)
- Komossa, S., Zhou, H., Wang, T., et al. 2008, *The Astrophysical Journal Letters*, 678, L13, doi: [10.1086/588281](https://doi.org/10.1086/588281)

- Liu, F. K., Li, S., & Chen, X. 2009, *ApJL*, 706, L133, doi: [10.1088/0004-637X/706/1/L133](https://doi.org/10.1088/0004-637X/706/1/L133)
- Liu, F. K., Li, S., & Komossa, S. 2014, *ApJ*, 786, 103, doi: [10.1088/0004-637X/786/2/103](https://doi.org/10.1088/0004-637X/786/2/103)
- MacLeod, C. L., Green, P. J., Anderson, S. F., et al. 2019, *ApJ*, 874, 8, doi: [10.3847/1538-4357/ab05e2](https://doi.org/10.3847/1538-4357/ab05e2)
- Malyali, A., Liu, Z., Rau, A., et al. 2023, *MNRAS*, 520, 3549, doi: [10.1093/mnras/stad022](https://doi.org/10.1093/mnras/stad022)
- Mandel, I., & Levin, Y. 2015, *ApJL*, 805, L4, doi: [10.1088/2041-8205/805/1/L4](https://doi.org/10.1088/2041-8205/805/1/L4)
- Nicastro, F. 2000, *The Astrophysical Journal Letters*, 530, L65, doi: [10.1086/312491](https://doi.org/10.1086/312491)
- Noda, H., & Done, C. 2018, *Monthly Notices of the Royal Astronomical Society*, 480, 3898, doi: [10.1093/mnras/sty2032](https://doi.org/10.1093/mnras/sty2032)
- Oehmamm, M. W., Kollatschny, W., Probst, M. A., et al. 2024, arXiv e-prints, arXiv:2402.12054, doi: [10.48550/arXiv.2402.12054](https://doi.org/10.48550/arXiv.2402.12054)
- Pan, X., Li, S.-L., & Cao, X. 2021, *The Astrophysical Journal*, 910, 97, doi: [10.3847/1538-4357/abe766](https://doi.org/10.3847/1538-4357/abe766)
- Park, T., Kashyap, V. L., Siemiginowska, A., et al. 2006, *ApJ*, 652, 610, doi: [10.1086/507406](https://doi.org/10.1086/507406)
- Payne, A. V., Shappee, B. J., Hinkle, J. T., et al. 2021, *ApJ*, 910, 125, doi: [10.3847/1538-4357/abe38d](https://doi.org/10.3847/1538-4357/abe38d)
- Penston, M. V., & Perez, E. 1984, *Monthly Notices of the Royal Astronomical Society*, 211, 33P, doi: [10.1093/mnras/211.1.33P](https://doi.org/10.1093/mnras/211.1.33P)
- Poole, T. S., Breeveld, A. A., Page, M. J., et al. 2008, *MNRAS*, 383, 627, doi: [10.1111/j.1365-2966.2007.12563.x](https://doi.org/10.1111/j.1365-2966.2007.12563.x)
- Rees, M. J. 1988, *Nature*, 333, 523, doi: [10.1038/333523a0](https://doi.org/10.1038/333523a0)
- . 1990, *Science*, 247, 817, doi: [10.1126/science.247.4944.817](https://doi.org/10.1126/science.247.4944.817)
- Rodríguez-Pascual, P. M., Alloin, D., Clavel, J., et al. 1997, *ApJS*, 110, 9, doi: [10.1086/312996](https://doi.org/10.1086/312996)
- Roming, P. W. A., Kennedy, T. E., Mason, K. O., et al. 2005, *Space Science Reviews*, 120, 95, doi: [10.1007/s11214-005-5095-4](https://doi.org/10.1007/s11214-005-5095-4)
- Roming, P. W. A., Koch, T. S., Oates, S. R., et al. 2009, *ApJ*, 690, 163, doi: [10.1088/0004-637X/690/1/163](https://doi.org/10.1088/0004-637X/690/1/163)
- Ross, N. P., Ford, K. E. S., Graham, M., et al. 2018, *Monthly Notices of the Royal Astronomical Society*, 480, 4468, doi: [10.1093/mnras/sty2002](https://doi.org/10.1093/mnras/sty2002)
- Runco, J. N., Cosens, M., Bennert, V. N., et al. 2016, *ApJ*, 821, 33, doi: [10.3847/0004-637X/821/1/33](https://doi.org/10.3847/0004-637X/821/1/33)
- Saxton, R. D., Motta, S. E., Komossa, S., & Read, A. M. 2015, *MNRAS*, 454, 2798, doi: [10.1093/mnras/stv2160](https://doi.org/10.1093/mnras/stv2160)
- Schlegel, D. J., Finkbeiner, D. P., & Davis, M. 1998, *ApJ*, 500, 525, doi: [10.1086/305772](https://doi.org/10.1086/305772)
- Sniegowska, M., Czerny, B., Bon, E., & Bon, N. 2020, *Astronomy & Astrophysics*, 641, A167, doi: [10.1051/0004-6361/202038575](https://doi.org/10.1051/0004-6361/202038575)
- Stone, N., & Loeb, A. 2011, *MNRAS*, 412, 75, doi: [10.1111/j.1365-2966.2010.17880.x](https://doi.org/10.1111/j.1365-2966.2010.17880.x)
- Takeuchi, S., Ohsuga, K., & Mineshige, S. 2013, *PASJ*, 65, 88, doi: [10.1093/pasj/65.4.88](https://doi.org/10.1093/pasj/65.4.88)
- Tananbaum, H., Avni, Y., Branduardi, G., et al. 1979, *ApJL*, 234, L9, doi: [10.1086/183100](https://doi.org/10.1086/183100)
- Truemper, J. 1982, *Advances in Space Research*, 2, 241, doi: [10.1016/0273-1177\(82\)90070-9](https://doi.org/10.1016/0273-1177(82)90070-9)
- Ulrich, M.-H., Maraschi, L., & Urry, C. M. 1997, *ARA&A*, 35, 445, doi: [10.1146/annurev.astro.35.1.445](https://doi.org/10.1146/annurev.astro.35.1.445)
- van Velzen, S., Pasham, D. R., Komossa, S., Yan, L., & Kara, E. A. 2021, *SSRv*, 217, 63, doi: [10.1007/s11214-021-00835-6](https://doi.org/10.1007/s11214-021-00835-6)
- Vaughan, S., Edelson, R., & Warwick, R. S. 2004, *MNRAS*, 349, L1, doi: [10.1111/j.1365-2966.2004.07615.x](https://doi.org/10.1111/j.1365-2966.2004.07615.x)
- Voges, W., Aschenbach, B., Boller, T., et al. 1999, *A&A*, 349, 389, doi: [10.48550/arXiv.astro-ph/9909315](https://doi.org/10.48550/arXiv.astro-ph/9909315)
- Wang, S., Woo, J.-H., Gallo, E., et al. 2024, arXiv e-prints, arXiv:2402.18131, doi: [10.48550/arXiv.2402.18131](https://doi.org/10.48550/arXiv.2402.18131)
- Webb, N. A., Barret, D., Godet, O., et al. 2023, *Astronomische Nachrichten*, 344, e20230051, doi: [10.1002/asna.20230051](https://doi.org/10.1002/asna.20230051)
- Wright, E. L. 2006, *The Publications of the Astronomical Society of the Pacific*, 118, 1711, doi: [10.1086/510102](https://doi.org/10.1086/510102)
- Xu, D. W., Komossa, S., Grupe, D., et al. 2024, *Universe*, 10, 61, doi: [10.3390/universe10020061](https://doi.org/10.3390/universe10020061)
- Zauderer, B. A., Berger, E., Soderberg, A. M., et al. 2011, *Nature*, 476, 425, doi: [10.1038/nature10366](https://doi.org/10.1038/nature10366)

APPENDIX

A. SWIFT OBSERVATIONS

Table 4. *Swift* XRT and UVOT observations of IC 3599 . The full machine-readable table is available on Zenodo: [10.5281/zenodo.10899673](https://zenodo.org/record/10899673)

Target ID	Segment	MJD ¹	T_{start} (UT)	T_{end} (UT)	T_{XRT}	T_{V}	T_{B}	T_{U}	T_{W1}	T_{M2}	T_{W1}
37507	001	55252.365	2010-02-25 07:46	2010-02-25 09:44	2120	176	176	176	352	486	704
	003	55333.049	2010-05-17 00:58	2010-05-17 01:19	1234	105	105	105	210	264	421
	004	56595.160	2013-10-30 00:34	2013-10-30 07:13	3771	312	312	312	624	795	1250
	005	56602.208	2013-11-06 02:24	2013-11-06 07:27	4832	—	—	—	—	4780	—
	006	56742.583	2014-03-26 07:50	2014-03-26 19:08	3596	101	101	101	204	2630	407
	37569	001	56877.306	2014-08-08 07:07	2014-08-08 07:35	1613	132	132	132	263	381
	002	56976.313	2014-11-15 04:12	2014-11-15 10:49	4615	107	107	3390	214	290	430
	003	56984.375	2014-11-23 08:57	2014-11-23 09:03	352	—	—	354	—	—	—
	004	57110.970	2015-03-29 21:37	2015-03-30 00:50	2829	229	229	229	460	675	920
	005	57209.167	2015-07-06 00:33	2015-07-06 04:08	4840	134	134	134	268	352	3740
	006	57215.146	2015-07-12 01:43	2015-07-12 06:40	1648	—	324	348	699	—	204
	007	57218.438	2015-07-15 07:57	2015-07-15 12:52	2377	193	193	193	387	528	779
	008	57220.604	2015-07-19 14:18	2015-07-19 14:44	1528	121	120	121	242	418	484
	009	57229.149	2015-07-26 02:37	2015-07-26 04:35	1913	158	158	158	317	430	635
	010	57236.194	2015-08-02 03:51	2015-08-02 05:43	1191	112	112	112	226	123	451
	011	57239.361	2015-08-05 08:34	2015-08-05 08:51	989	81	81	81	160	240	322
	012	57243.316	2015-08-09 05:01	2015-08-09 10:11	2000	164	164	164	328	471	658
	013	57327.104	2015-11-01 00:03	2015-11-01 05:20	4697	130	132	132	3370	379	527
	014	57387.375	2015-12-31 04:27	2015-12-31 13:43	3385	—	—	—	1915	—	—
	015	57466.333	2016-03-19 00:44	2016-03-19 15:11	4014	105	105	105	211	3010	423
	016	57589.506	2016-07-20 11:54	2016-07-20 12:22	1663	136	136	136	272	409	545
	017	57590.399	2016-07-21 07:10	2016-07-21 12:02	3274	264	264	264	530	783	1058
	018	57762.924	2017-01-09 20:44	2016-01-09 23:42	2412	135	135	135	270	1142	539
	019	57765.253	2017-01-12 03:03	2017-01-12 06:10	2515	75	75	75	149	236	1873
	020	57798.750	2017-02-14 14:34	2017-02-14 21:11	1543	117	117	117	234	441	469
	021	57810.667	2017-02-26 10:34	2017-02-26 23:30	1471	117	117	117	231	352	463
	022	57826.507	2017-03-12 12:13	2017-03-12 12:19	3446	—	—	81	259	—	—
	023	57828.439	2017-03-16 08:53	2017-03-16 12:11	1735	140	140	140	280	414	561
	024	57838.632	2017-03-26 14:11	2017-03-26 16:05	2008	165	165	165	329	459	661
	025	57852.750	2017-04-09 03:30	2017-04-09 08:25	1331	105	106	106	212	304	425
	026	57866.910	2017-04-23 21:37	2017-04-23 22:05	1623	134	134	134	268	390	537
	027	57880.552	2017-05-07 06:05	2017-05-07 20:25	1918	155	155	155	310	462	622
	028	57894.899	2017-05-21 04:42	2017-05-22 13:12	2093	169	169	169	338	515	677
	029	57908.858	2017-06-04 19:50	2017-06-04 21:32	1216	107	107	145	313	78	429
	030	57969.344	2017-08-04 00:09	2017-08-04 16:16	2115	171	171	171	273	482	547
	031	58065.042	2017-11-08 00:03	2017-11-08 01:42	1756	150	150	150	300	514	600
10375	001	58072.705	2017-11-15 15:17	2017-11-15 18:35	3718	249	381	381	763	689	1144
	002	58076.618	2017-11-19 14:40	2017-11-19 14:59	1139	96	96	96	193	233	386
	003	58103.928	2017-12-16 22:12	2017-12-16 22:24	694	60	60	60	121	172	242
	004	58105.486	2017-12-17 23:38	2017-12-18 23:41	4078	340	340	340	679	922	1361
	005	58133.514	2018-01-15 05:01	2018-01-15 19:37	4545	347	347	410	832	1056	1390
	006	58164.500	2018-02-15 02:23	2018-02-15 21:45	4825	388	388	388	776	1131	1554
	007	58192.318	2018-03-15 01:09	2018-03-15 14:04	4730	390	387	390	785	983	1567
	008	58223.566	2018-04-15 09:35	2018-04-15 17:44	4877	405	405	405	811	1042	1625
	009	58253.625	2018-05-15 13:10	2018-05-15 16:43	2944	233	233	233	469	731	935
	010	58256.708	2018-05-18 16:07	2018-05-18 17:57	1830	89	170	170	341	263	681
	011	58284.448	2018-06-15 08:57	2018-06-15 12:29	4935	481	407	407	813	1134	1628
	012	58315.421	2018-07-15 22:05	2018-07-16 22:10	4635	362	362	362	727	1139	1455

¹ The Modified Julian Date (MJD) is given for the middle of the observation period.

Table 1. Continued

Target ID	Segment	MJD ¹	T_{start} (UT)	T_{end} (UT)	T_{XRT}	T_{V}	T_{B}	T_{U}	T_{W1}	T_{M2}	T_{W1}
10375	013	58339.170	2018-08-09 02:18	2018-08-09 05:52	4580	235	235	235	469	749	941
	014	58422.882	2018-10-31 18:52	2018-10-31 23:30	4949	397	397	397	794	1205	1592
	015	58423.389	2018-11-01 05:48	2018-11-01 12:42	5002	413	413	413	828	1107	1659
	016	58452.387	2018-11-30 09:22	2018-11-30 14:31	4540	350	317	362	724	1122	1450
	017	58453.542	2018-12-01 15:35	2018-12-01 17:31	2532	207	207	207	414	584	829
	018	58482.979	2018-12-30 22:31	2018-12-31 00:34	3219	268	268	268	536	772	1074
	019	58488.059	2019-01-05 01:14	2019-01-05 01:34	1209	101	101	101	203	258	405
	020	58492.747	2019-01-09 17:04	2019-01-09 18:47	862	—	180	180	361	—	98
	021	58496.694	2019-01-13 16:27	2019-01-13 16:51	1409	115	115	115	230	331	460
	022	58500.344	2019-01-17 01:46	2019-01-17 15:02	4755	386	386	386	775	1059	1552
	023	58514.403	2019-01-31 00:42	2019-01-31 20:01	1306	82	141	141	331	219	331
	024	58519.486	2019-02-05 03:41	2019-02-05 19:33	1928	146	146	146	393	439	586
	025	58521.085	2019-02-08 01:33	2019-02-08 03:22	1726	140	140	140	281	392	563
	026	58531.542	2019-02-17 06:50	2019-02-17 15:06	4448	362	362	362	727	999	1457
	027	58546.101	2019-03-03 13:25	2019-03-04 15:03	4902	398	398	398	802	1169	1604
	028	58559.278	2019-03-17 00:54	2019-03-17 12:19	3652	263	263	263	531	765	1059
	029	58573.531	2019-03-31 09:13	2019-03-31 16:07	4817	396	396	396	795	1056	1590
	030	58590.403	2019-04-17 04:26	2019-04-17 14:20	4880	391	391	390	786	1190	1575
	031	58620.403	2019-05-17 06:22	2019-05-17 13:00	3985	323	323	323	645	931	1293
	032	58634.524	2019-05-31 02:07	2019-05-31 23:16	2869	164	280	280	684	392	921
	033	58651.483	2019-06-17 03:25	2019-06-17 07:15	4905	403	403	403	803	1149	1610
	034	58665.295	2019-07-01 02:05	2019-07-01 12:04	4001	348	348	348	696	663	1397
	035	58681.139	2019-07-17 00:46	2019-07-17 06:00	4470	369	369	369	739	1015	1479
	036	58704.569	2019-08-09 01:34	2019-08-10 01:53	3861	225	225	225	500	736	906
	037	58788.138	2019-11-01 01:32	2019-11-01 05:07	4253	345	345	345	690	1024	1381
	038	58808.292	2019-11-21 04:22	2019-11-21 09:35	3047	250	250	250	499	714	999
	040	58814.549	2019-11-27 00:37	2019-11-28 02:23	4192	346	346	346	693	943	1387
	041	58834.819	2019-12-17 16:26	2019-12-17 22:58	3696	181	376	376	751	612	1372
	042	58865.354	2020-01-17 00:33	2019-01-17 16:40	2642	237	237	237	474	413	947
	044	58886.552	2020-02-07 06:49	2019-02-07 19:45	2113	171	172	172	343	465	689
	045	58909.708	2020-03-01 13:39	2019-03-01 20:23	2315	188	188	188	376	548	751
	046	58943.500	2020-04-03 23:27	2020-04-04 23:34	2233	182	182	182	365	514	731
	047	58970.292	2020-05-01 01:19	2020-05-01 12:39	2068	166	166	166	333	474	668
	048	59001.656	2020-06-01 15:51	2020-06-01 16:02	642	53	54	54	107	125	214
	049	59002.426	2020-06-02 06:10	2020-06-02 14:19	1129	87	87	87	178	280	349
	050	59031.104	2020-07-01 00:07	2020-07-01 05:06	1743	144	144	144	288	377	575
	051	59062.650	2020-08-01 14:37	2020-08-01 16:37	2290	187	187	187	374	534	747
	052	59154.500	2020-11-01 03:58	2020-11-01 20:03	1935	158	158	158	315	439	632
	053	59184.813	2020-12-01 17:02	2020-12-01 22:02	1626	134	134	134	306	344	534
	054	59188.892	2020-12-05 21:13	2020-12-05 21:35	1291	107	107	107	214	286	428
	055	59215.674	2021-01-01 15:10	2021-01-01 17:11	3042	246	246	246	493	739	985
	056	59246.594	2021-02-01 02:47	2021-02-01 23:47	3112	245	245	245	491	788	985
	057	59274.087	2021-02-28 22:01	2021-03-01 06:11	1973	159	159	159	317	469	637
	058	59305.792	2021-04-01 18:45	2021-04-01 20:37	1201	98	98	98	195	256	393
	059	59340.125	2021-05-06 02:18	2021-05-06 04:10	1538	122	122	122	243	381	485
	061	59372.774	2021-06-06 05:26	2021-06-07 21:42	1713	132	132	132	265	425	532
	062	59374.155	2021-06-09 03:38	2021-06-09 03:48	567	45	45	45	89	131	179
	063	59378.597	2021-06-13 14:15	2021-06-13 14:28	789	62	62	62	125	197	249

¹ The Modified Julian Date (MJD) is given for the middle of the observation period.

Table 1. Continued

Target ID	Segment	MJD ¹	T_{start} (UT)	T_{end} (UT)	T_{XRT}	T_V	T_B	T_U	T_{W1}	T_{M2}	T_{W1}
10375	064	59396.359	2021-07-01 06:07	2021-07-01 11:08	1508	118	118	118	237	375	474
	065	59427.389	2021-08-01 05:56	2021-08-01 12:38	2290	182	182	182	362	580	725
	066	59522.399	2021-11-04 06:55	2021-11-04 12:10	3366	273	273	273	548	812	1096
	067	59527.740	2021-11-09 12:47	2021-11-09 22:45	2277	180	180	180	360	572	721
	068	59552.469	2021-12-04 05:47	2021-12-04 18:37	2605	178	247	284	568	526	710
	069	59556.222	2021-12-08 05:19	2021-12-08 05:23	245	—	—	34	203	—	—
	070	59560.128	2021-12-12 02:54	2021-12-12 03:13	1126	94	94	94	188	239	377
	071	59583.910	2022-01-04 21:02	2022-01-04 23:07	3479	281	281	281	563	853	1128
	073	59674.611	2022-04-05 13:46	2022-04-05 15:34	1181	91	91	91	183	296	366
	074	59703.993	2022-05-04 05:44	2022-05-04 12:02	1888	146	146	146	294	435	588
	075	59704.432	2022-05-05 10:27	2022-05-05 16:43	1721	141	141	141	281	380	563
	076	59734.146	2022-06-03 17:50	2022-06-04 11:25	2375	197	197	197	396	514	792
	077	59764.390	2022-07-04 06:08	2022-07-04 12:37	4163	328	328	328	656	1063	1313
	078	59795.644	2022-08-04 01:49	2022-08-04 21:04	3334	266	266	266	530	779	1064
	079	59883.310	2022-10-31 07:19	2022-10-31 15:47	2055	175	175	175	348	416	693
	080	59914.585	2022-12-01 03:09	2022-12-01 20:59	1024	44	89	181	363	122	179
	081	59919.955	2022-12-06 22:51	2022-12-06 22:56	405	—	69	69	138	—	109
	082	59923.339	2022-12-10 08:05	2022-12-10 08:12	414	37	37	37	75	49	150
	083	59936.658	2022-12-23 15:34	2022-12-23 16:03	1716	141	141	141	280	404	562
	084	59944.535	2022-12-31 12:37	2022-12-31 13:04	1576	135	135	135	270	318	539
	085	59948.812	2023-01-04 18:54	2023-01-04 20:05	817	—	157	157	314	—	145
	086	59949.630	2023-01-05 15:00	2023-01-05 15:16	913	79	79	79	157	192	315
	087	59950.838	2023-01-06 19:59	2023-01-06 20:15	926	76	76	76	151	211	303
	088	59951.623	2023-01-07 14:49	2023-01-07 15:05	844	71	71	71	142	172	283
	089	59952.411	2023-01-08 09:51	2023-01-08 10:05	804	65	65	65	130	187	261
	090	59953.011	2023-01-09 00:09	2023-01-09 00:23	794	70	70	70	139	134	278
	091	59954.007	2023-01-10 00:05	2023-01-10 00:17	694	71	71	71	142	30	283
	092	59955.596	2023-01-11 14:11	2023-01-11 14:25	819	69	69	69	137	163	276
	093	59956.868	2023-01-12 20:42	2023-01-12 20:58	914	75	75	75	149	202	300
	094	59957.791	2023-01-13 18:52	2023-01-13 19:06	824	67	67	67	134	188	269
	095	59964.619	2023-01-20 06:52	2023-01-20 22:51	1156	97	97	97	194	221	389
	096	59974.341	2023-01-30 08:05	2023-01-30 08:17	660	68	68	68	136	—	272
	097	59975.276	2023-01-31 06:30	2023-01-31 09:57	1503	46	170	170	341	156	564
	098	59977.793	2023-02-02 18:59	2023-02-02 19:08	534	47	47	47	93	81	188
	099	59984.472	2023-02-09 11:14	2023-02-09 11:25	642	50	50	50	100	160	201
	100	59994.269	2023-02-19 06:21	2023-02-19 06:34	789	68	68	68	136	143	272
	101	60004.532	2023-03-01 12:41	2023-03-01 12:51	604	54	54	54	108	87	216
	102	60009.765	2023-03-06 18:14	2023-03-06 18:31	979	—	128	128	257	—	439
	103	60014.532	2023-03-11 07:54	2023-03-11 17:38	1174	101	101	101	201	202	403
	104	60024.925	2023-03-21 22:05	2023-03-21 22:19	821	66	66	66	132	195	264
	105	60034.588	2023-03-31 07:46	2023-03-31 20:29	1400	122	122	122	244	238	489
	106	60044.968	2023-04-10 23:05	2023-04-10 23:24	1096	90	90	90	182	240	364
	107	60054.563	2023-04-20 13:24	2023-04-20 13:38	817	68	68	68	137	168	273
	108	60065.357	2023-05-01 08:21	2023-05-01 08:48	1613	132	132	132	264	384	527
	109	60095.205	2023-05-31 04:05	2023-05-31 05:46	1214	159	65	65	318	408	637
	110	60126.288	2023-07-01 02:52	2023-07-01 10:58	1900	165	165	165	328	348	657
	111	60156.127	2023-07-31 02:50	2023-07-31 03:16	1518	124	124	124	249	358	498

¹ The Modified Julian Date (MJD) is given for the middle of the observation period.

Table 2. Merged XRT data as shown in Figure 6

MJD Range	MJD _{center}	bin width ¹	$F_{0.3-10keV}^2$	HR ³
56595 - 57243	56916.0	648.0	0.943±0.120	+0.00±0.10
57327 - 57969	57648.0	642.0	0.906±0.100	-0.36±0.15
58065 - 58339	58202.0	137.0	0.615±0.059	-0.22±0.12
58422 - 58704	58563.0	141.0	1.008±0.065	-0.39±0.12
58788 - 59062	58925.0	137.0	1.870±0.131	-0.66±0.07
59154 - 59427	59290.5	136.5	2.170±0.219	-0.54±0.07
59527 - 59795	59661.0	134.0	3.080±0.260	-0.36±0.08
59883 - 59975 ⁴	59929.0	46.0	4.557±0.817	-0.68±0.05
59977 - 60065 ⁵	60021.0	44.0	1.340±0.558	+0.22±0.18

¹ given in days

² The observed 0.3-10 keV fluxes are given in units of 10^{-16} W m⁻².

³ The hardness ratio is defined as $HR = \frac{hard-soft}{hard+soft}$ with the soft and hard bands in the 0.3-1.0 and 1.0-10 keV bands, respectively, applying the BEHR program by citetpark2006

⁴ The data from the mini flare in December 2022.

⁵ After flare data from February to May 2023

Table 3. *Swift* XRT and UVOT fluxes of IC 3599 The full machine-readable table is available on Zenodo: [10.5281/zenodo.10899673](https://zenodo.org/record/10899673).

MJD	$F_{0.3-10\text{keV}}^1$	HR ²	F_V^3	F_B^3	F_U^3	F_{W1}^3	F_{M2}^3	F_{W2}^3
55252.365	105.8±6.00	-0.91±0.03	13.03±0.48	10.01±0.37	7.25±0.27	5.83±0.21	5.69±0.26	5.13±0.19
55333.049	29.09±3.14	-0.86±0.07	11.77±0.55	9.47±0.35	6.80±0.25	5.22±0.24	5.48±0.31	5.04±0.23
56595.160	1.15±0.45 ⁴	-0.18±0.30	8.85±0.33	7.31±0.27	3.60±0.16	2.71±0.12	2.24±0.12	2.39±0.08
56602.208	1.08±0.40 ⁴	—	—	—	—	—	2.50±0.09	—
56742.583	0.73±0.33 ⁴	—	9.52±0.53	7.45±0.27	3.91±0.18	2.66±0.17	2.48±0.09	2.45±0.13
56877.306	—	—	9.35±0.43	7.18±0.26	3.77±0.17	2.79±0.15	2.62±0.17	2.52±0.11
56976.188	1.51±0.40 ⁴	—	9.10±0.51	7.66±0.35	3.56±0.13	2.38±0.15	2.02±0.15	2.28±0.12
57110.970	0.47±0.22 ⁴	—	8.77±0.32	6.92±0.25	3.43±0.16	2.36±0.13	2.08±0.11	2.08±0.09
57209.167	—	—	9.35±0.43	7.52±0.28	3.53±0.16	2.89±0.16	2.74±0.18	2.47±0.09
57215.146	1.40±0.75 ⁴	—	—	6.98±0.26	3.53±0.13	2.52±0.11	—	2.32±0.15
57218.438	1.00±0.55 ⁴	—	9.02±0.42	7.18±0.26	3.34±0.15	2.66±0.15	2.32±0.15	2.36±0.11
57220.604	1.55±0.75 ⁴	—	9.53±0.44	7.18±0.26	3.73±0.17	2.52±0.16	2.53±0.16	2.59±0.14
57229.149	1.15±0.75 ⁴	—	8.53±0.39	7.38±0.34	3.70±0.17	2.69±0.15	2.80±0.18	2.54±0.11
57236.194	1.55±1.12 ⁴	—	9.71±0.54	7.80±0.36	3.63±0.20	2.61±0.17	2.74±0.26	2.30±0.13
57239.361	2.90±1.20 ⁴	—	9.80±0.55	7.80±0.36	3.34±0.22	3.03±0.20	2.43±0.18	2.52±0.14
57243.316	—	—	9.80±0.45	7.59±0.28	3.77±0.17	2.74±0.15	2.53±0.16	2.59±0.12
57327.104	0.86±0.20 ⁴	—	9.35±0.52	7.25±0.27	3.53±0.19	2.59±0.09	2.72±0.18	2.45±0.13
57387.375	1.35±0.45 ⁴	0.01±0.37	—	—	—	2.71±0.10	—	—
57466.333	0.68±0.30 ⁴	—	8.53±0.48	6.67±0.31	3.43±0.16	2.47±0.16	2.46±0.06	2.32±0.13
57590.500	1.00±0.35 ⁴	-0.11±0.35	9.27±0.34	7.18±0.26	3.60±0.13	2.76±0.12	2.48±0.14	2.39±0.11
57762.924	3.76±1.01 ⁴	-0.59±0.17	9.35±0.43	7.18±0.26	3.84±0.18	2.71±0.17	2.39±0.11	2.59±0.12
57765.253	—	—	9.80±0.55	6.79±0.31	3.80±0.21	2.74±0.18	2.50±0.19	2.15±0.80
57798.750	—	—	9.71±0.45	7.45±0.27	3.84±0.18	2.74±0.18	2.24±0.14	2.62±0.14
57810.667	2.15±1.00 ⁴	—	10.16±0.47	7.38±0.27	4.13±0.19	2.89±0.19	2.65±0.07	2.54±0.14
57826.507	1.76±0.81 ⁴	—	8.69±0.40	7.31±0.27	3.98±0.18	2.79±0.15	2.82±0.18	2.69±0.12
57838.632	—	—	8.93±0.41	7.18±0.26	3.53±0.16	2.57±0.14	2.65±0.17	2.36±0.11
57852.750	1.82±1.69 ⁴	—	9.62±0.54	7.11±0.26	3.43±0.19	2.52±0.16	2.46±0.16	2.32±0.13
57866.910	1.49±1.07 ⁴	—	9.53±0.44	7.18±0.26	3.91±0.18	2.89±0.16	2.60±0.17	2.47±0.14
57880.552	—	—	9.71±0.45	6.92±0.25	3.40±0.15	2.89±0.16	2.22±0.14	2.32±0.10
57894.899	2.14±0.81 ⁴	—	8.61±0.40	7.18±0.26	3.77±0.17	2.74±0.15	2.50±0.16	2.52±0.11
57908.858	—	—	9.62±0.54	7.38±0.27	3.63±0.17	2.84±0.16	2.28±0.31	2.36±0.13
57969.344	1.81±0.81 ⁴	—	9.35±0.43	7.05±0.26	3.63±0.17	2.64±0.17	—	2.57±0.12
58065.042	—	—	9.10±0.51	6.92±0.25	3.34±0.15	2.19±0.12	1.99±0.13	1.73±0.97
58072.705	1.50±0.54 ⁴	—	9.62±0.35	7.11±0.26	3.56±0.13	2.57±0.12	2.48±0.14	2.30±0.10
58076.618	—	—	9.98±0.56	6.73±0.31	3.84±0.21	2.52±0.16	2.48±0.18	2.36±0.13
58103.928	—	—	10.30±0.78	7.11±0.40	4.05±0.26	2.81±0.21	2.87±0.24	2.10±0.13
58105.486	1.18±0.46 ⁴	—	9.01±0.33	7.18±0.26	3.60±0.13	2.50±0.11	2.55±0.11	2.45±0.09
58133.514	—	—	9.27±0.34	7.11±0.26	3.56±0.13	2.57±0.12	2.50±0.11	2.47±0.09
58164.500	1.02±0.43 ⁴	-0.63±0.37	9.35±0.34	7.18±0.26	3.70±0.13	2.57±0.12	2.67±0.12	2.66±0.09
58192.318	1.74±0.46 ⁴	-0.31±0.24	8.93±0.33	7.11±0.26	3.77±0.14	2.59±0.12	2.57±0.12	2.54±0.09
58223.566	1.58±0.52 ⁴	-0.57±0.32	9.27±0.34	7.11±0.26	3.80±0.14	2.61±0.12	2.48±0.11	2.43±0.09
58253.625	2.12±0.70	-0.32±0.30	9.89±0.36	7.38±0.27	3.66±0.13	2.81±0.13	2.53±0.14	2.54±0.11
58256.708	1.48 ⁴ ±0.90	—	9.62±0.54	7.05±0.26	3.87±0.18	2.69±0.15	2.57±0.17	2.45±0.11
58284.448	1.05±0.58	+0.03±0.26	9.10±0.33	7.38±0.27	3.66±0.13	2.79±0.13	2.55±0.11	2.54±0.09
58315.421	0.83±0.30 ⁴	-0.48±0.36	9.53±0.35	7.31±0.27	3.77±0.17	2.74±0.12	2.57±0.12	2.45±0.06

¹ The observed 0.3-10 keV fluxes are given in units of 10^{-16} W m⁻².² The hardness ratios are as defined in Table 2³ The Fluxes in the UVOT filters are given in units of 10^{-15} W m⁻².⁴ 0.3-10 keV fluxes estimated from the course rates based on the latest possible spectral analysis.

Table 3. Continued

MJD	$F_{0.3-10\text{keV}}^1$	HR ²	F_V^3	F_B^3	F_U^3	F_{W1}^3	F_{M2}^3	F_{W2}^3
58339.170	0.64±0.25	-0.46±0.22	10.30±0.38	7.05±0.26	3.98±0.18	2.71±0.15	2.80±0.15	2.66±0.12
58422.882	—	—	9.44±0.35	7.11±0.26	3.80±0.17	2.69±0.12	2.67±0.12	2.54±0.09
58423.389	0.68±0.23 ⁴	-0.44±0.23	9.62±0.54	7.18±0.26	3.87±0.14	2.66±0.12	2.50±0.11	2.52±0.09
58452.387	1.36±0.45 ⁴	-0.66±0.28	9.35±0.34	7.11±0.26	3.66±0.13	2.64±0.12	2.37±0.11	2.50±0.09
58453.542	1.29±0.40 ⁴	-0.30±0.19	9.89±0.36	7.25±0.27	3.53±0.13	2.61±0.14	2.48±0.14	2.47±0.11
58482.979	1.50±0.50 ⁴	-0.47±0.25	9.80±0.36	7.18±0.26	3.60±0.16	2.81±0.13	2.69±0.15	2.47±0.11
58488.059	—	—	10.25±0.57	7.66±0.28	3.80±0.21	2.54±0.16	2.57±0.17	2.54±0.14
58492.747	—	—	—	7.11±0.26	3.77±0.17	2.74±0.15	—	2.57±0.24
58496.694	—	—	10.25±0.48	7.05±0.33	4.21±0.19	2.79±0.18	2.55±0.16	2.64±0.14
58500.344	0.93±0.31 ⁴	-0.75±0.15	9.44±0.35	7.18±0.26	3.84±0.14	2.59±0.12	2.57±0.12	2.45±0.09
58514.403	1.41±0.52 ⁴	+0.12±0.34	9.62±0.54	7.31±0.27	3.84±0.18	2.66±0.15	2.32±0.17	2.64±0.14
58519.486	1.41±0.35	-0.96±0.04	9.27±0.43	7.31±0.27	3.87±0.18	2.69±0.15	2.48±0.16	2.69±0.12
58521.085	—	—	9.89±0.46	7.73±0.28	3.91±0.18	2.76±0.15	2.57±0.17	2.54±0.11
58531.542	1.08±0.26 ⁴	-0.63±0.20	9.61±0.35	7.31±0.27	3.84±0.18	2.81±0.13	2.41±0.11	2.47±0.09
58546.101	1.78±0.30	-0.30±0.24	9.98±0.27	7.31±0.27	3.91±0.14	2.74±0.12	2.37±0.11	2.62±0.09
58559.278	1.45±0.50 ⁴	-0.20±0.32	9.53±0.35	7.31±0.27	3.91±0.14	2.76±0.12	2.46±0.13	2.39±0.11
58573.531	1.38±0.38 ⁴	-0.15±0.28	9.35±0.34	7.18±0.26	3.56±0.13	2.66±0.12	2.48±0.11	2.43±0.09
58590.403	2.31±0.42	-0.95±0.05	9.18±0.34	7.31±0.27	3.73±0.13	2.54±0.11	2.43±0.11	2.43±0.09
58620.403	2.05±0.63 ⁴	-0.45±0.27	9.53±0.35	7.31±0.27	3.77±0.17	2.61±0.12	2.55±0.11	2.39±0.08
58634.524	1.15±0.45 ⁴	-0.87±0.13	9.27±0.43	7.45±0.27	3.73±0.13	2.79±0.13	2.50±0.16	2.52±0.11
58651.483	1.81±0.50	-0.07±0.21	9.62±0.35	7.38±0.27	3.84±0.14	2.66±0.12	2.62±0.12	2.50±0.09
58665.295	1.98±0.69	-0.51±0.23	9.02±0.33	7.05±0.26	3.47±0.12	2.64±0.12	2.28±0.12	2.28±0.08
58681.139	0.96±0.32 ⁴	+0.30±0.35	9.27±0.34	7.38±0.27	3.60±0.13	2.64±0.12	2.28±0.10	2.28±0.08
58704.569	0.58±0.31 ⁴	-0.42±0.24	9.44±0.35	7.38±0.27	4.02±0.18	2.71±0.12	2.62±0.14	2.45±0.11
58788.138	2.04±0.45	-0.91±0.09	9.71±0.36	7.45±0.27	3.70±0.17	2.71±0.12	2.60±0.12	2.41±0.90
58808.292	1.77±0.54	-0.47±0.29	9.98±0.37	7.11±0.26	3.80±0.17	2.59±0.12	2.50±0.14	2.50±0.11
58814.549	3.32±0.67	-0.67±0.16	10.16±0.37	7.31±0.27	3.87±0.18	2.74±0.12	2.46±0.11	2.52±0.09
58834.819	1.04±0.42 ⁴	+0.06±0.38	9.53±0.44	7.45±0.27	3.77±0.14	2.57±0.12	2.53±0.14	2.36±0.08
58865.354	1.82±0.66 ⁴	-0.71±0.29	9.62±0.35	7.38±0.27	3.70±0.13	2.57±0.14	2.41±0.13	2.26±0.10
58886.552	3.28±0.88 ⁴	-0.76±0.24	10.25±0.48	7.45±0.27	3.91±0.18	2.69±0.15	2.74±0.18	2.66±0.12
58909.708	3.16±0.88 ⁴	-0.35±0.25	9.71±0.45	7.25±0.27	4.17±0.15	2.79±0.15	2.85±0.16	2.64±0.12
58943.500	1.93±0.81 ⁴	-0.95±0.05	9.35±0.43	7.59±0.28	4.21±0.15	2.84±0.16	2.50±0.14	2.47±0.11
58970.292	2.78±0.96 ⁴	-0.78±0.23	9.44±0.71	8.02±0.45	4.13±0.27	2.43±0.20	2.72±0.26	2.45±0.16
59002.426	4.75±1.73	-0.79±0.21	10.54±0.59	7.45±0.34	3.98±0.22	2.76±0.18	2.46±0.16	2.45±0.16
59031.104	2.64±0.79 ⁴	—	9.62±0.45	7.59±0.28	4.02±0.18	2.79±0.18	2.32±0.15	2.59±0.12
59062.650	1.17±0.37 ⁴	-0.72±0.28	8.30±0.46	5.50±0.25	2.51±0.21	2.38±0.18	2.55±0.16	2.39±0.11
59154.500	1.92±0.60	-0.58±0.22	9.80±0.45	7.38±0.27	4.05±0.19	2.66±0.15	2.53±0.16	2.43±0.11
59184.813	0.75±0.35 ⁴	—	9.02±0.50	6.92±0.25	3.91±0.18	2.57±0.14	2.37±0.15	2.36±0.13
59188.892	1.95±0.48 ⁴	—	9.80±0.55	7.80±0.29	3.80±0.21	2.66±0.17	2.65±0.17	2.28±0.12
59215.674	1.97±0.73 ⁴	—	9.44±0.35	7.38±0.27	3.66±0.13	2.74±0.12	2.48±0.14	2.39±0.11
59246.594	1.66±0.60	-0.29±0.24	9.62±0.35	7.11±0.26	3.91±0.14	2.79±0.13	2.62±0.14	2.69±0.12
59274.087	0.86±0.39 ⁴	—	9.44±0.44	7.38±0.27	3.60±0.16	2.38±0.15	2.26±0.15	2.28±0.10
59305.792	1.83±0.71 ⁴	—	9.80±0.55	7.45±0.34	3.56±0.20	2.66±0.20	2.32±0.17	2.59±0.14
59340.125	1.41±0.52 ⁴	—	9.62±0.45	7.52±0.28	3.80±0.17	2.45±0.16	2.26±0.15	2.26±0.12
59372.774	1.18±0.41 ⁴	-0.20±0.30	9.27±0.43	7.38±0.27	3.73±0.17	2.81±0.18	2.65±0.22	2.54±0.14
59374.155	—	—	9.53±0.72	7.52±0.42	4.45±0.33	2.92±0.25	2.24±0.23	2.26±0.17

¹ The observed 0.3-10 keV fluxes are given in units of 10^{-16} W m⁻².² The hardness ratio is defined as $HR = \frac{\text{hard-soft}}{\text{hard+soft}}$ with the soft and hard bands in the 0.3-1.0 and 1.0-10 keV bands, respectively, applying the BEHR program by [Park et al. \(2006\)](#)³ The Fluxes in the UVOT filters are given in units of 10^{-15} W m⁻².⁴ 0.3-10 keV fluxes estimated from the count rates based on the latest possible spectral analysis.

Table 3. Continued

MJD	$F_{0.3-10\text{keV}}^1$	HR ²	F_V^3	F_B^3	F_U^3	F_{W1}^3	F_{M2}^3	F_{W2}^3
59378.597	—	—	9.44±0.62	6.92±0.39	3.56±0.27	2.71±0.20	2.77±0.21	2.69±0.15
59396.359	2.60±0.78 ⁴	-0.51±0.22	9.89±0.46	7.73±0.36	3.53±0.19	2.57±0.17	2.62±0.17	2.66±0.15
59427.389	2.12±0.95	-0.97±0.03	10.16±0.47	7.31±0.34	4.02±0.18	2.74±0.15	2.57±0.14	2.69±0.12
59522.399	1.61±0.40	-0.38±0.22	9.71±0.36	7.25±0.33	3.80±0.14	2.54±0.11	2.43±0.13	2.26±0.10
59527.740	2.59±0.62	-0.61±0.18	9.53±0.44	7.18±0.33	3.80±0.17	2.52±0.14	2.41±0.13	2.22±0.10
59552.469	2.75±0.74	+0.18±0.18	8.85±0.41	7.18±0.33	3.60±0.13	2.79±0.13	2.69±0.15	2.34±0.11
59556.222	—	—	—	—	3.84±0.36	2.76±0.18	—	—
59560.128	—	—	9.02±0.50	6.86±0.32	3.80±0.21	2.34±0.15	2.35±0.20	2.10±0.13
59583.910	1.41±0.41	-0.40±0.22	9.62±0.35	7.31±0.27	3.73±0.17	2.71±0.12	2.62±0.12	2.47±0.11
59674.611	3.67±2.33 ⁴	-0.65±0.35	10.74±0.60	7.25±0.33	3.28±0.18	2.59±0.17	2.55±0.16	2.39±0.13
59703.993	2.52±0.80 ⁴	-0.20±0.22	9.02±0.42	7.18±0.33	3.91±0.18	2.76±0.15	2.65±0.14	2.50±0.11
59734.146	2.75±0.99	-0.25±0.23	10.16±0.37	7.38±0.27	3.80±0.14	2.84±0.16	2.57±0.14	2.59±0.12
59764.390	5.00±0.53	-0.54±0.12	9.98±0.37	7.38±0.27	3.91±0.14	2.71±0.12	2.53±0.11	2.47±0.09
59795.644	2.96±0.70	-0.38±0.21	9.98±0.37	7.31±0.27	3.80±0.14	2.66±0.12	2.39±0.13	2.34±0.11
59883.310	4.65±0.44	-0.63±0.18	9.52±0.45	7.45±0.28	3.67±0.17	2.37±0.13	2.53±0.17	2.24±0.11
59914.585	1.41±0.11 ⁴	—	8.61±0.74	7.59±0.36	3.57±0.17	2.69±0.15	2.12±0.25	2.20±0.17
59919.955	6.27±3.41 ⁴	—	—	6.93±0.39	3.77±0.25	2.14±0.18	—	2.48±0.21
59923.339	12.93±4.50 ⁴	-0.59±0.25	9.27±0.80	7.32±0.48	3.57±0.31	1.99±0.23	2.68±0.42	2.08±0.18
59936.658	4.49±1.21 ⁴	-0.79±0.20	9.98±0.47	7.59±0.28	3.99±0.19	2.62±0.15	2.46±0.16	2.50±0.14
59944.535	8.89±2.05 ⁴	-0.76±0.12	10.16±0.48	7.39±0.28	3.60±0.17	2.82±0.16	2.55±0.17	2.46±0.14
59948.812	5.82±2.20 ⁴	-0.79±0.21	—	6.99±0.26	3.57±0.17	2.43±0.16	—	2.16±0.19
59949.630	9.92±1.39	-0.83±0.16	9.18±0.61	7.32±0.34	4.17±0.24	2.62±0.17	2.51±0.22	2.39±0.16
59950.838	6.52±1.75 ⁴	-0.81±0.19	9.18±0.61	7.25±0.34	3.28±0.22	2.74±0.18	2.37±0.20	2.18±0.14
59951.623	8.64±2.03 ⁴	-0.70±0.18	8.77±0.58	6.67±0.38	3.95±0.22	2.43±0.19	2.46±0.21	2.26±0.15
59952.411	7.13±2.15 ⁴	-0.74±0.21	9.89±0.65	6.86±0.39	3.64±0.24	3.01±0.23	2.70±0.23	2.18±0.17
59953.011	6.43±2.03 ⁴	-0.64±0.21	8.22±0.54	7.66±0.36	3.32±0.22	2.20±0.17	1.96±0.21	1.93±0.15
59954.007	4.43±2.21 ⁴	-0.68±0.32	9.35±0.62	7.52±0.36	3.70±0.26	2.57±0.20	2.16±0.48	2.24±0.13
59955.596	6.49±2.15 ⁴	-0.51±0.22	10.64±0.60	6.86±0.39	3.44±0.23	2.67±0.20	2.27±0.22	2.24±0.15
59956.868	8.37±2.52	-0.40±0.21	9.98±0.66	7.59±0.36	3.77±0.25	2.67±0.20	2.05±0.20	2.20±0.15
59957.791	5.25±3.70 ⁴	—	9.02±0.60	7.05±0.40	3.50±0.23	2.72±0.21	2.49±0.21	2.30±0.15
59964.619	6.62±1.70	-0.26±0.23	9.02±0.51	7.12±0.33	3.95±0.22	2.62±0.20	2.25±0.19	2.35±0.13
59974.341	6.61±2.79 ⁴	-0.26±0.35	10.16±0.67	6.86±0.39	3.81±0.25	2.55±0.19	—	2.37±0.16
59975.276	5.03±1.67 ⁴	-0.33±0.25	9.53±0.72	7.32±0.27	3.84±0.18	2.57±0.15	2.53±0.22	2.48±0.14
59977.793	—	—	11.25±0.75	6.93±0.39 ⁴	3.74±0.28	2.84±0.24	2.44±0.33	2.48±0.16
59984.472	4.67±2.09 ⁴	+0.16±0.37	9.27±0.71	7.81±0.44	3.77±0.29	2.69±0.23	2.60±0.22	2.50±0.17
59994.269	7.28±3.70 ⁴	—	10.07±0.67	7.88±0.37	3.60±0.24	2.87±0.22	2.37±0.23	2.46±0.16
60004.532	—	—	10.74±0.71	7.52±0.43	4.17±0.28	2.52±0.22	2.99±0.35	2.24±0.15
60009.765	—	—	—	6.93±0.26	3.64±0.17	2.32±0.15	—	2.10±0.12
60014.532	2.79±1.15 ⁴	+0.09±0.31	9.18±0.52	7.25±0.34	3.84±0.22	2.59±0.17	2.18±0.19	2.46±0.14
60024.925	—	—	8.38±0.55	7.25±0.34	3.54±0.23	2.55±0.19	1.94±0.17	2.18±0.14
60034.588	3.52±1.15 ⁴	+0.73±0.25	9.10±0.43	7.12±0.27	3.57±0.17	2.59±0.17	2.48±0.21	2.06±0.12
60044.968	—	—	9.98±0.56	7.45±0.35	4.10±0.23	2.67±0.18	2.21±0.17	2.22±0.15
60054.563	2.78±1.44 ⁴	+0.06±0.42	9.89±0.65	6.86±0.39	3.08±0.20	2.64±0.23	2.56±0.22	2.22±0.15
60065.357	1.38±0.77 ⁴	+0.33±0.36	9.10±0.43	7.32±0.27	3.88±0.18	2.30±0.15	2.42±0.16	2.37±0.14
60095.205	4.22±1.60 ⁴	-0.02±0.31	8.85±0.42	8.03±0.45	3.91±0.26	—	2.18±0.15	—
60126.288	3.95±1.11 ⁴	-0.31±0.26	9.80±0.46	7.32±0.27	3.67±0.17	2.62±0.15	2.32±0.15	2.30±0.13
60156.127	1.89±0.99 ⁴	-0.46±0.54	9.36±0.53	6.55±0.31	3.70±0.21	2.67±0.18	2.42±0.16	2.30 ±0.13

¹ The observed 0.3-10 keV fluxes are given in units of 10^{-16} W m⁻².² The hardness ratio is defined as $HR = \frac{\text{hard-soft}}{\text{hard+soft}}$ with the soft and hard bands in the 0.3-1.0 and 1.0-10 keV bands, respectively, applying the BEHR program by [Park et al. \(2006\)](#)³ The Fluxes in the UVOT filters are given in units of 10^{-15} W m⁻².⁴ 0.3-10 keV fluxes estimated from the count rates based on the latest possible spectral analysis.

Table 4. Merged UVOT data as shown in Figure 7.

MJD Range	MJD _{center}	bin width ¹	F_V^2	F_B^2	F_U^2	F_{W1}^2	F_{M2}^2	F_{W2}^2
56595 - 57590	57092.5	497.5	9.22±0.26	7.23±0.21	3.56±0.10	2.59±0.08	2.53±0.08	2.37±0.07
57762 - 57969	57865.5	103.5	9.24±0.26	7.07±0.21	3.67±0.11	2.76±0.10	2.56±0.10	2.39±0.07
58065 - 58339	58202.0	137.0	9.30±0.18	7.07±0.21	3.64±0.11	2.63±0.08	2.58±0.10	2.43±0.07
58422 - 58704	58563.0	141.0	9.40±0.18	7.20±0.21	3.74±0.11	2.70±0.08	2.54±0.07	2.43±0.07
58788 - 59062	58925.0	137.0	9.57±0.27	7.25±0.21	3.92±0.11	2.73±0.08	2.61±0.10	2.43±0.10
59154 - 59427	59290.5	136.5	9.46±0.27	7.25±0.21	3.74±0.11	2.68±0.11	2.54±0.10	2.47±0.10
59527 - 59795	59661.0	134.0	9.51±0.27	7.20±0.21	3.74±0.11	2.68±0.08	2.56±0.10	2.35±0.07
59883 - 60156	60019.5	136.5	9.51±0.28	7.29±0.21	3.71±0.11	2.55±0.10	2.45±0.10	2.20±0.09
56595 - 60156	58375.5	1780.5	9.45±0.23	7.15±0.14	3.68±0.11	2.66±0.09	2.55±0.06	2.42±0.06

¹ given in days² The reddening-corrected UVOT fluxes are given in units of 10^{-15} W m⁻².